

Heat transfer enhancement of twisted tape inserts in supercritical carbon dioxide flow conditions based on CFD and vortex kinematics

Wenguang Li^a, Zhibin Yu^{a,*}, Yi Wang^b, Yongliang Li^b

^a School of Engineering, University of Glasgow, G12 8QQ Glasgow, UK

^b School of Chemical Engineering, University of Birmingham, B15 2TT Birmingham, UK

ARTICLE INFO

Keywords:

Twisted tape insert
Supercritical carbon dioxide
Computational fluid dynamics
Vortex kinematics
Heat transfer enhancement
Performance evaluation criterion

ABSTRACT

Twisted tape inserts (TTI) are often employed to enhance heat transfer in tubes but their enhancement for supercritical carbon dioxide (SCO₂) is unknown, and the thermal performance of TTIs is never studied by vortex kinematics. The TTIs with three twist ratios (TR) were designed for an experimental SCO₂ water-cooled counter-flow tube-in-tube heat exchanger, and the convective heat transfer of SCO₂ in the exchangers with the TTIs was simulated with ANSYS CFX based on the three-dimensional, Reynolds-averaged Navier-Stokes equations, energy equation and shear stress transport turbulence model. Effects of TR, mass flux, inlet pressure and wall heat flux on the performance were clarified. The optimal TRs were sought by using the performance evaluation criterion curve and criterion of friction factor ratio ≤ 5 . The thermal performance was characterised by using cross-sectional average absolute helicity. The friction factor ratio, Nusselt number ratio and performance evaluation criterion vary in the ranges of 3.63–7.29, 3.43–5.75 and 1.90–2.94 at the pseudocritical point, inlet pressure of 8, 9 MPa, mass flux of 200, 400 kg/m²s and wall heat flux of 12, 24 kW/m² as TR = 2.17, 3.78, 5.39. The best heat transfer enhancement caused by TTIs appears at the point with 2–3 times better than that in water or air flow. The enhancement reduces dramatically on the left- and right-hand sides of the point. The increased mass flux and inlet pressure can reduce but a large wall flux can raise the enhancement on both sides of the point. The optimal TR depends on SCO₂ operational conditions and TR = 3.78 is the optimal TR for most cases herein.

1. Introduction

Water-cooled supercritical carbon dioxide (SCO₂) heat exchangers (HX) can find an application in cooling or cold storage systems using carbon dioxide (CO₂) hydrate slurry as a working fluid and storage medium. The thermophysical properties of SCO₂ vary considerably with temperature and pressure, especially near the critical point or pseudocritical point. Because SCO₂ is subject to a lower overall heat transfer coefficient (HTC) than water, SCO₂ convective heat transfer in a SCO₂ HX needs to be enhanced to improve its effectiveness and reduce its size. However, heat transfer enhancement (HTE) techniques in water-cooled SCO₂ counter-flow tube-in-tube heat exchangers have been rarely investigated so far. For example, 52, 46, and 50 spiral fins were manufactured inside a tube with 4.42 mm inner diameter in 24, 5 and 25° helix angles, and the convective heat transfer of SCO₂ was measured at 8–10 MPa and 20–75°C inlet temperature as well as 360–690 kg/(m²s) mass flux in [1]. It turned out that the HTC in the finned tubes was 1.4–2.0 times better than that in the smooth tube. In similar

experimental work [2], the HTC was improved by 20–39% only.

For fluids with constant thermophysical properties, the other HTE methods were proposed to enhance their forced convective heat transfer in HXs. Basically, four kinds of HTE methods, namely dimple, protrusion, twisted tape insert and rough element methods exist for HXs. An array of outward dimples is made on the inner wall of a tube in the dimple method, and the convective heat transfer over the wall is enhanced by vortices generated by those dimples. Usually, the shape of dimples is partially spherical, but an outward dimple with a small inward dimple in it could improve convective heat transfer further [3]. The thermal-hydraulic performance of teardrop shape dimples was better than that of spherical dimples based on simulations of computational fluid dynamics (CFD) [4,5] and experiments [6]. For spherical dimples, the depth of the dimples influenced their thermal-hydraulic performance greatly [7]. In the protrusion method, an array of inward protrusions is created on the inner wall of a tube, and the convective heat transfer over the wall is improved. The shape of protrusions is often partially spherical [8,9]. However, the other shapes, such as teardrop [5], elliptical [10], and slot [11] were also suggested and exhibited a

* Corresponding author.

E-mail address: Zhibin.Yu@glasgow.ac.uk (Z. Yu).

<https://doi.org/10.1016/j.tsep.2022.101285>

Received 17 December 2021; Received in revised form 22 February 2022; Accepted 27 March 2022

Available online 31 March 2022

2451-9049/© 2022 The Author(s). Published by Elsevier Ltd. This is an open access article under the CC BY license (<http://creativecommons.org/licenses/by/4.0/>).

Nomenclature			
a	constant in the μ_t expression of the shear stress transport model, $a = 0.31$	z	axial coordinate of twisted tape insert, mm
A	overall heat exchange area in a heat exchanger, m^2	<i>Greek</i>	
B	constant in log-law velocity profile, $B = 5.2$ for hydraulically smooth walls	$\alpha_1, \beta_1, \sigma_{\omega 1}$	model constants in the ω -equation of the Wilcox $k-\omega$ model, $\alpha_1=5/9, \beta_1=0.075, \sigma_{\omega 1}=2$
C_p	specific heat capacity of fluid, J/kg	$\alpha_2, \beta_2, \sigma_{\omega 2}$	model constants in the ω -equation of the ω -transformed standard $k-\varepsilon$ model, $\alpha_2=0.44, \beta_2=0.0828, \sigma_{\omega 2}=1/0.856$
d	tube inner diameter, mm	$\alpha_3, \beta_3, \sigma_{\omega 3}$	blended model constants in the ω -equation of the blended Wilcox $k-\omega$ and standard $k-\varepsilon$ models, $\alpha_3=F_1\alpha_1+(1-F_1)\alpha_2, \beta_3=F_1\beta_1+(1-F_1)\beta_2, \sigma_{\omega 3}=F_1\sigma_{\omega 1}+(1-F_1)\sigma_{\omega 2}$
d_w	tape width, mm	β	auxiliar variable in dimensionless fluid temperature expression in the boundary layer
f	friction factor of a tube with heat transfer enhancement	β_k	model constant in the k -equation of the Wilcox $k-\omega$ model and the ω -transformed standard $k-\varepsilon$ model, $\beta_k=0.09$
f_0	friction factor of a tube without heat transfer enhancement	γ	magnitude of the strain rate of fluid velocity, 1/s
F_1	blending function between the Wilcox $k-\omega$ model and the standard $k-\varepsilon$ model	γ_{ij}	strain rate tensor of fluid velocity, 1/s
F_2	auxiliary variable in the μ_t expression of the shear stress transport model	Γ	auxiliary variable dimensionless fluid temperature in boundary layer
G	mass flux, $kg/m^2 s$	δ	tape thickness, mm
h	specific enthalpy of fluid, m^2/s^2	Δ	discriminant defined by I_1, I_2, I_3 in Eq. (22)
H	absolute helicity of fluid, m/s^2	Δp_{tot}	difference in the total pressure of SCO ₂ across the tube with TTI, Pa
H_b	cross-sectional mean absolute helicity, m/s^2	ε	dissipation rate of turbulence kinetic energy, m^2/s^3
H_{b1}	cross-sectional mean absolute helicity at the inlet of twisted tape insert, m/s^2	ϵ_{ijm}	Levi-Civita symbol, $i, j, m=1, 2, 3$
I_1, I_2, I_3	Invariants of velocity gradient tensor defined by Eq.(21)	κ	von Kármán constant, $\kappa=0.41$
k	turbulence kinetic energy, m^2/s^2	λ	thermal conductivity of fluid, W/m K
l	total axial length of a tape, mm	λ_b	mean bulk thermal conductivity of SCO ₂ in the tube with TTI, W/m K
Nu	Nusselt numbers with (after) heat transfer enhancement	μ	dynamic viscosity of fluid, Pa.s
Nu_0	Nusselt numbers without (before) heat transfer enhancement	μ_t	turbulent eddy viscosity, Pa.s
p	fluid static pressure, MPa	ν	kinematic viscosity of fluid, m^2/s
$P_{kb}, P_{\omega b}$	buoyancy production term in the k -equation and ω -equation, respectively, J/m^3	ξ_1, ξ_2	auxiliary variables in the F_1 expressions
Pr	fluid Prandtl number	ξ_3	auxiliary variable in the μ_t expression of the shear stress transport model
Pr_t	turbulent Prandtl number, $Pr_t=0.9$	ρ	density of fluid, kg/m^3
q_w	water heat flux across the tube wall, kW/m^2	ρ_b	mean bulk density of SCO ₂ in the tube with TTI, kg/m^3
Re	Reynolds number at the inlet of tube	σ_{k1}	model constant in the k -equation of the Wilcox $k-\omega$ model, $\sigma_{k1}=2$
S_E	source term of energy equation, J/m^3	σ_{k2}	model constant in the k -equation of the standard $k-\varepsilon$ model, $\sigma_{k2}=1$
S_i	specific body force, $i=1, 2, 3, m/s^2$	σ_{k3}	blended model constant in the k -equation of the blended Wilcox $k-\omega$ and standard $k-\varepsilon$ models, $\sigma_{k3}=F_1\sigma_{k1}+\beta_1(1-F_1)\sigma_{k2}$
t	time, s	τ_w	wall shear stress, Pa
\angle	pitch of a twisted tape insert in 180° turning angle of the tape, mm	ψ	performance evaluation criterion for heat transfer enhancement
T	local temperature of fluid, K	Y	swirling strength of the vortex expressed by Eq. (23), 1/s
T_1	fluid temperature at inlet of the tube, K	ω	rate of dissipation per unit turbulent kinetic energy, 1/s
T_b	mean bulk temperature of fluid, K	ω_n	total ω near wall, 1/s
T_c	temperature at pseudo critical point of fluid, K	$\omega_{log}, \omega_{vis}$	ω values calculated by the solutions in the logarithmic and linear near-wall regions, 1/s
T_n	fluid temperature in the first mesh layer, K	Ω	vorticity or velocity curl of fluid, 1/s
T_{nw}	wall adjacent temperature, K	Ω_b	cross-sectional mean velocity curl, 1/s
T_w	mean or local wall temperature, K	<i>Subscript</i>	
T^+	dimensionless temperature in the boundary layer	i, j, m	index of the Cartesian coordinate system
u	fluid velocity vector, m/s	<i>Abbreviation</i>	
u_b	bulk velocity of SCO ₂ in the tube with TTI, m/s	3D	three-dimensional
u_i, u_j	Reynolds time-averaged velocity components of fluid in a Cartesian coordinate system, $i, j=1,2, 3, m/s$	CFD	computational fluid dynamics
u_n	fluid velocity near wall, m/s	CO ₂	carbon dioxide
u_τ	friction velocity of fluid at wall, $\tau_w = \rho u_\tau^2, m/s$	HX	heat exchanger
u_i'	turbulent fluctuation velocity of fluid, m/s	HTC	heat transfer coefficient
$u_\tau^{log}, u_\tau^{vis}$	friction velocities at wall by using the solutions in the log-law and sublayer layers	HTE	heat transfer enhancement
U	mean heat transfer coefficient, W/m^2K	PEC	performance evaluation criterion
U_w	wall heat transfer coefficient, W/m^2K		
U_{wb}	cross-sectional mean wall heat transfer coefficient, W/m^2K		
x_i, x_j, x_m	coordinates of a Cartesian coordinate system, $i, j, m=1, 2, 3, m$		
y_n	distance to the nearest wall from the first mesh layer, m		
y^+	dimensionless wall distance, $y^+ = \sqrt{\tau_w/\rho} y_n/\nu$		

PCHE	printed circuit heat exchanger	SCO ₂	supercritical carbon dioxide
RANS	Reynolds-averaged Navier-Stokes equations	SST	shear stress transport
RGP	real gas property		

better HTC in comparison with spherical protrusions. The protrusions in spherical shape were applied into the HX in a solar water heater [12] and nanofluids [13]. The arrays of the dimples/protrusions with elliptical, conical frustum, trapezoidal prism, leeward triangular and upward triangular shapes were created in each fin plate in a fin-and-elliptical HX, respectively, and the convective heat transfer in the HX was simulated with CFD software [14]. In the twisted tape insert (TTI) method, a single TTI [15] or more TTIs in series [16] or in parallel [17] were installed in a tube to generate a vortex flow and enhance HTC. The effect of tape aspect (length-to-width) ratio on the thermal-hydraulic performance of TTIs was predicted with CFD and it turned out that HTE was elevated with increasing aspect ratio [18]. There are a variety of mutated TTIs, for instance, centrally hollowed TTIs [19], coaxially crossed TTIs [20], eccentric helical screw tape insert where the tape is twisted helically on a cylindrical surface [21], helical screw tape inserts where the tape is twisted helically on a straight rod [22], tape with holes [23], and tape with a linearly variable pitch [24]. A triple-channel TTI was assembled into a three-start spirally twisted tube, their effect on HTC was predicted with CFD software [25]. TTIs were also used to enhance HTC in HXs working in TiO₂/water [17], Fe₃O₄/water [26] nanofluids. In the rough element method, a series of rough elements with sharp or blunt shapes was installed in a tube or on its wall to intensify the turbulent kinetic energy level of fluid and enhance the fluid HTC over the wall. There are a large number of types of rough elements proposed in the literature, e.g., dividing turbulators in tube [27], twisted ribs on tube wall [28], vortex generators on wall [29], winglet vortex generator on tube wall [30], helical V-grooves on tube wall [31], airfoil deflectors in tube [32], spiral spring inserts [33], louvred strip inserts [34], longitudinal strip inserts in tube [35], transverse ribs on tube wall [36], conical ribs on tube wall [37], and curved circular rings in tube [38] to name a few. Various vortex generators were reviewed in-depth based on their configurations and thermal-hydraulic performance [39]. A comparison of the thermal-hydraulic performance of dimples, cylindrical grooves and short fins in mini-channel heat sinks was conducted based on CFD simulations [40]. The transverse ribs with rectangular, trapezoidal, semi-circular and triangular cross-sections on tube wall were designed and the convective heat transfer in the tubes with those ribs was simulated with CFD software Fluent and compared with the heat transfer in the tubes with outward protrusions in those cross-sections [41]. A TTI was installed in a tube with protrusions on tube wall, and the convective heat transfer and thermal-hydraulic performance of the TTI were predicted with CFD simulations [42]. A TTI was combined with vortex generating rings and installed in a tube to enhance HTC and the geometric parameters of the rings were optimised by using the response surface method based on the data obtained with CFD simulations [43].

Compared with dimples, protrusions and rough elements, TTIs are usually installed inside a circular plain tube of HX with a radial gap and don't reduce the mechanical strength of the tube wall, thus they are suitable for working in a tube with high internal pressure. Further, TTIs are subject to simple structure and easy fabrication, and have found extensive applications in air conditioning and refrigeration systems, chemical reactors, food and dairy processes [44]. However, the thermal-hydraulic performance of an HX with TTI is almost associated with the convective heat transfer of fluids with nearly constant thermophysical properties presently [45]. Hence, there is no information about the thermal-hydraulic performance of TTIs under convective heat transfer conditions of SCO₂ which undergoes significant thermophysical

property variation in the vicinity of its pseudocritical points. Also, there is a lack of methods for characterising the thermal performance of a TTI which is associated with a strong swirling flow from the vortex kinematics point of view in the literature. These two issues will be addressed herein.

In this article, three TTIs were designed for an experimental water-cooled counter-flow tube-in-tube HX, and the convective heat transfer between SCO₂ and the tube in each HX with a TTI was investigated numerically in CFD software-ANSYS CFX 2019R2a by using three-dimensional (3D) Reynolds-averaged Navier-Stokes equations (RANS), energy equation and shear stress transport (SST) turbulence flow model for the first time. The effects of twist ratio (TR), SCO₂ inlet pressure, mass flux, and wall heat flux on HTE were explored based on the simulated results, and the optimal TR was sought. The vortex region was identified with absolute helicity, and the cross-sectional mean wall HTC was correlated with the helicity to characterise the thermal performance of a TTI. The studied issues are unseen in the literature, the corresponding outcomes will be beneficial to the design and experiment of TTIs and can shed light on the flow and heat transfer mechanisms of TTIs.

2. Design of TTI

2.1. Selection of SCO₂ HX

In our one project, the water-cooled HX will run in the following conditions: SCO₂ inlet pressure $p_1 = 7\text{--}10$ MPa, temperature $T_1 = 30\text{--}70$ °C, mass flux $G = 200\text{--}850$ kg/m²s, cooling water inlet temperature = 10–20 °C, pressure = 1 atm. Operating pressure and temperature, cost, fouling and cleanability, fluid leakage and contamination, fluids and material compatibility, and fluid type are factors to consider when deciding the selection criteria of HX [46], among which operating pressure, temperature, cost, and fluid type are more important to the project. Based on the operating pressure and temperature, a counter-flow tube-in-tube HX or printed circuit heat exchanger (PCHE) can be selected. However, PCHEs are subject to a higher cost and a larger pressure loss, as such the counter-flow tube-in-tube HX has to be selected.

The counter-flow tube-in-tube HX is a gas-to-liquid HX. The HTC on the gas side is smaller than that on the liquid side in the HX. To align the magnitude in UA on each fluid side of the HX, an HTE method should be applied to the gas side, here U is the mean HTC and A is the overall heat transfer area.

2.2. Geometry of TTI

Four HTE methods, namely dimple, protrusion, TTI and rough element methods, may be potentially applicable to SCO₂ counter-flow tube-in-tube HXs [45]. Since the fabrication of TTIs is easier than that of dimples, protrusions and rough elements, and the TTIs do not impair the mechanical strength of the tube wall to allow a tube to be safer at a higher internal pressure, the HTE of TTI will be examined under SCO₂ flow conditions here.

A notable drawback of TTI may be the larger flow resistance to the flow. A gap between TTI and tube wall or holes in the tape can intensify turbulent level and alleviate the larger flow resistance, thus could lead to enhance heat transfer at the tube wall inside the HX. The best thermal performance in HTE of TTIs was achieved at $Re = 7200\text{--}49,800$ [44],

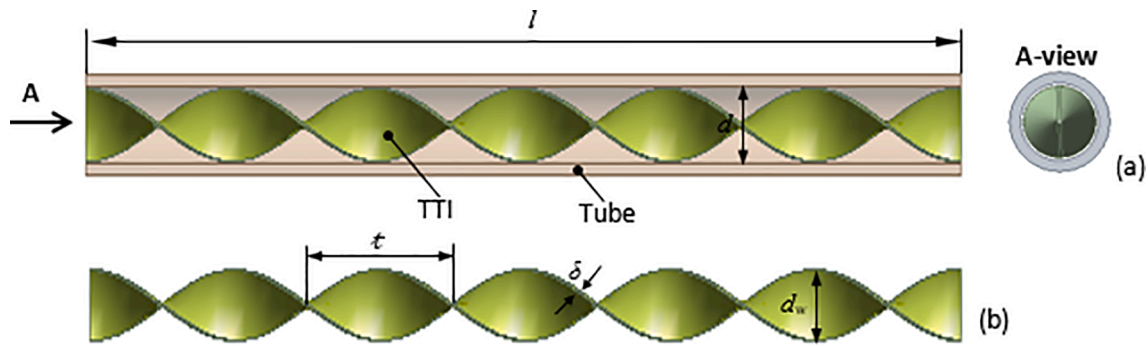


Fig. 1. The geometrical parameters representing a twisted tape insert, (a) assembling of tube and twisted tape insert, (b) the insert with geometrical dimensions.

where there is a gap between the insert and the tube, and the tape is perforated. The principal geometrical parameters of the insert are shown in Fig. 1. Note the TTI used in this study is imperforated considering computing resource limitations, but the findings can serve as the foundation and guidance of more complex numerical simulation of perforated TTIs in the future.

The geometrical parameters of the insert used here, namely the pitch l (tape turning 180°), tape width d_w , tape thickness δ are scaled from the tape in [44]. The aspect ratio l/d_w of the tape in [44] and that here is not scalable. The geometrical parameters of the insert here are tabulated in Table 1 and compared with the original parameters in [44]. Note that the feasible t or TR l/d_w will be determined by using ψ and f/f_0 values in the given range of Reynolds number based on CFD simulation results, where f and f_0 denote the friction factors with and without HTE and the performance evaluation criterion (PEC) ψ is defined as:

$$\psi = \frac{Nu/Nu_0}{(f/f_0)^{1/3}} \quad (1)$$

where Nu and Nu_0 represent the Nusselt numbers with and without HTE.

To determine a suitable range of TR , a survey on TR values in the literature was carried out, and the TR profile, mean and standard deviation are illustrated in Fig. 2 based on TR values in [44,47–55] under heat transfer conditions of fluids with constant thermophysical properties. It is shown that the TR in these studies is 3.78 ± 1.61 . Accordingly, three values $2.17(=3.78-1.61)$, 3.78 and $5.39(=3.78 + 1.61)$ are selected and tabulated in Table 1 for the TTI design in the present study.

2.3. Fluid domain, mesh, flow models and boundary conditions

The convective heat transfer and turbulent flow of SCO_2 in an experimental counter-flow tube-in-tube HX without TTI were investigated numerically in [56] and validated with the experimental data in [57]. Therefore, the same HX is employed here again to clarify the effect of TTI on HTE under SCO_2 convective heat transfer conditions. The experimental counter-flow tube-in-tube HX with a 500 mm long TTI is shown in Fig. 3. The twisted tape was generated by using the Sweep method in ANSYS DesignModeler. The geometrical parameters of the TTIs are listed in Table 1. The HX is represented by the sole tube model [56] to form the computational model with HTE element.

In the sole tube model, there are the upstream and downstream tubes with adiabatic walls, and the inner wall at which a known outward uniform wall heat flux q_w caused by a counter-flow of chilly water in the

jacket outside the tube is enforced. At the inlet of the upstream tube, the pressure p_1 and temperature T_1 of SCO_2 are known, while the mass flow rate of SCO_2 is prescribed with $\pi G d^2/4$ at the outlet of the downstream tube, where G is SCO_2 mass flux, and d is tube inner diameter ($d = 6$ mm). The fluid domain is the fluid enclosed by the inner walls of the gas side tube and insert, the inlet, and the outlet, as shown in Fig. 3.

The CFD software ANSYS CFX 2019R2 was adopted to perform SCO_2 heat transfer simulations in the HX with TTI. The SCO_2 simulated here is compressible gas, its thermophysical properties depend on both temperature and pressure. The flow of SCO_2 is 3D, steady and turbulent, its governing equations and SST turbulence model are demonstrated in Appendix A.

Based on the real gas property (RGP) table, the SCO_2 thermophysical property constants are interpolated with local temperature and pressure in the simulated fluid domain using the REFPROP Version 9.0 program issued by the National Institute of Standards and Technology.

Totally, twelve cases were investigated to examine the HTE behavior of the TTI under various conditions of SCO_2 mass flux, inlet temperature, inlet pressure and wall heat flux as well as TR , which are summarised in Table 2. The corresponding results of simulation in the same inlet flow and thermal conditions and geometrical parameters of the HX with plain tube (without TTI) were presented in [56] and will be used as the basis to evaluate the HTE of TTI.

The boundary layer y^+ value is critical to heat transfer simulation of SCO_2 flow in a tube, and the accuracy of heat transfer prediction depends on the inflation mesh size near a wall. For the SST model, when y^+ was in the range of 1–3, the HTC predicted was in good agreement with the experimental data in both sides of the pseudocritical point [58,59,56]. In this regard, inflation meshes near the tube and TTI walls were paved with the first layer height of 0.005 mm compared with 0.004 mm in the HX tube without TTI. The resulted y^+ is in the range of 1.6–4.0 at $G = 200$ kg/m²s and $p_1 = 8$ MPa, 2.2–6.0 at $G = 400$ kg/m²s and $p_1 = 8$ MPa, 1.3–3.0 at $G = 400$ kg/m²s and $p_1 = 9$ MPa, respectively. In most cases, the boundary layer y^+ is in the range of 1–3 basically. The detailed information about meshes can be found in Table 3. A close-up of the mesh at $TR = 3.78$ is illustrated in Fig. 4.

In the flow and heat transfer simulations, the governing equations in Appendix A are discretised by using the finite volume method. Since the flow and heat transfer are steady, the temporal terms in the equations are eliminated. The convection terms in the RANS equation are approximated with the 2nd-order difference scheme (the high-order scheme in CFX), while the convection terms in the SST model equation are done with the 1st-order scheme. The diffusion terms in the governing equations are discretised with the 2nd-order central difference scheme. The tolerance residuals of convergence are selected to be 1×10^{-5} for all the variables.

The SCO_2 temperature and pressure are provided at the inlet to the tube, while the mass flow rate of SCO_2 is specified at the outlet. A known outward constant wall heat flux (negative value) is given on the 500 mm long cylindrical surface shown in Fig. 3. The rest surfaces are under

Table 1

The geometrical parameters of the twisted tape inserts.

Source	d (mm)	d_w (mm)	l (mm)	δ (mm)	l (mm)	l/d_w
[44]	70	65	1500	3	124.8	1.92
Present	6	5.57	500	0.257	10.70	2.17, 3.78, 5.39

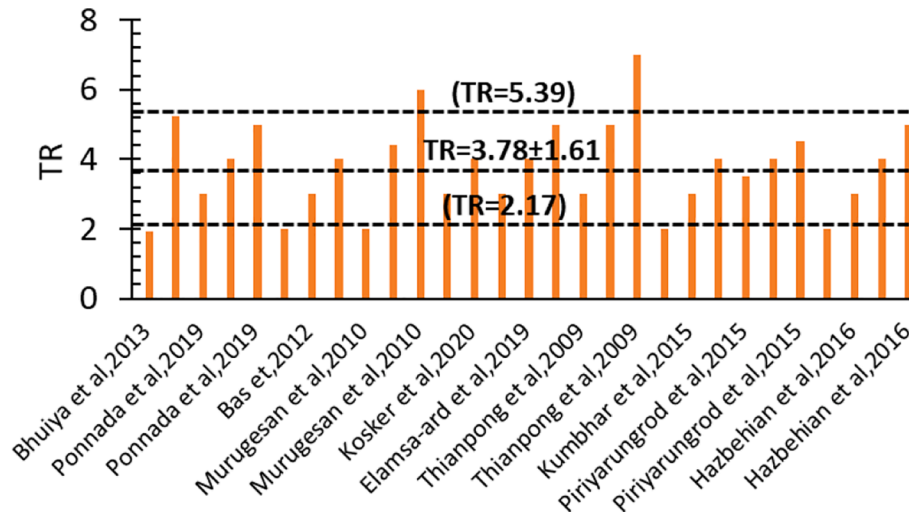


Fig. 2. The TR profile, mean and standard deviation, the TR values are obtained from [44,47-55].

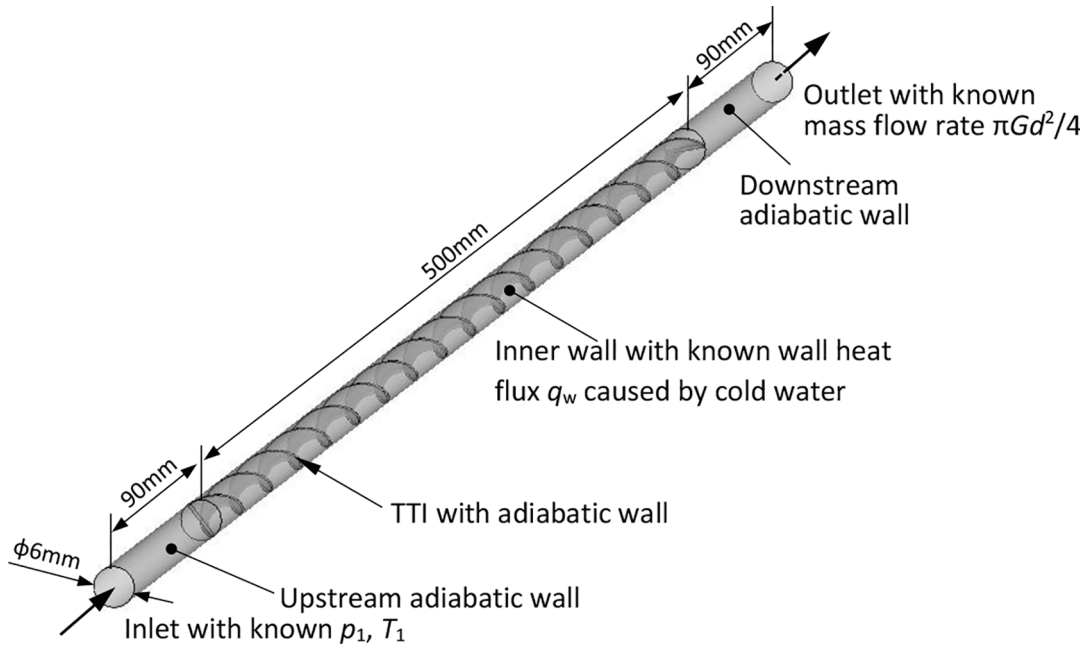


Fig. 3. The fluid domain of an experimental counter-flow tube-in-tube heat exchanger of SCO₂ with TTI.

adiabatic conditions. CFX expression language is employed to calculate SCO₂ mass flow rate and apply those conditions to the boundaries.

In the case of TR = 3.78, a fine mesh presented in Table 3 was created as well. The mean SCO₂ shear stress τ_w and temperature T_w at the tube wall in the fair and fine meshes are given in Fig. 4 as a function of SCO₂ mean bulk temperature T_b . The two variables show little variation with the mesh size; thus, the fair mesh is adopted in the following CFD simulations.

3. Results

3.1. Overall performance of TTI

The overall performance of an HX with TTI is characterised by contrasting the hydraulic and thermal performance of the HX with TTI against the corresponding performance of the HX without TTI. The variables describing the overall performance include the friction factor ratio f/f_0 and the Nusselt number ratio Nu/Nu_0 as well as the PEC ψ

between the two HXs. Based on these variables, the optimal TRs can be determined. These variables will be demonstrated under various conditions of TR, mass flux, inlet pressure and wall flux in the following sections. The friction factor f and Nusselt number Nu in the HX with TTI are calculated by using the following expressions:

$$\begin{cases} f = \frac{\Delta p_{tot}}{\rho_b \left(\frac{l}{d}\right) \left(\frac{1}{2}u_b^2\right)} \\ Nu = \left(\frac{q_w}{T_b - T_w}\right) \frac{d}{\lambda_b} \end{cases} \quad (2)$$

where Δp_{tot} is the difference in the total pressure of SCO₂ flowing across the tube with TTI, ρ_b and u_b are the mean bulk density and bulk velocity of SCO₂ in the tube with TTI, T_b and T_w are the mean bulk temperature of SCO₂ in the tube with TTI and the mean wall temperature, λ_b is the mean bulk thermal conductivity of SCO₂ in the tube with TTI. Those parameters were extracted from the CFX result files in CFX-Post. The

Table 2

The cases studied in the SCO₂ heat transfer simulations for the HXs with TTI.

Inner diameter, <i>d</i> (mm)	TR	Mass flux, <i>G</i> (kg/m ² s)	Wall heat flux, <i>q_w</i> (kW/m ²)	Inlet pressure, <i>p</i> ₁ (MPa)	Inlet temperature, <i>T</i> ₁ (°C)
6	2.17,3.78,5.39	200	12	8	26–65
			24		30–70
		400	12		26–60
			12	9	22.5–70

calculating expressions for *f*₀ and *Nu*₀ are the same as *f* and *Nu*, except for using the values of total pressure, mean bulk parameters and wall temperature in the HX without TTI.

The *f*₀ and *Nu*₀ values in the HX without TTI were predicted with the same method here by employing Mesh2 in Table 3, and are illustrated in Fig. 5 in terms of the mean bulk temperature *T*_b and Reynolds number *Re*. The details of the CFD simulations can be referred to [56]. Those *f*₀ and *Nu*₀ will be used to calculate the ratios *f*/*f*₀, *Nu*/*Nu*₀ and PEC *ψ* to assess the HTE of TTI at the same *T*_b and *Re*.

In these curves, *f*₀ rises steadily with decreasing *T*_b or *Re*; *Nu*₀, however, arrives at the maximum values at the pseudocritical points, and then levels off with increasing or decreasing *T*_b and *Re*.

3.1.1. Effects of SCO₂ mass flux

The friction factor ratio *f*/*f*₀, Nusselt number ratio *Nu*/*Nu*₀, and PEC *ψ* at two mass fluxes *G* = 200, 400 kg/m²s, inlet pressure *p*₁ = 8 MPa and wall heat flux *q*_w = 12 kW/m² are plotted as a function of SCO₂ mean bulk temperature *T*_b in Fig. 6(a)–(c). To identify the features in the *f*/*f*₀, *Nu*/*Nu*₀ and *ψ* curves, the experimental data of the *f*/*f*₀, *Nu*/*Nu*₀ and *ψ* on common fluids such as air [44] and water [55], respectively, are illustrated in the figure based on the Reynolds number *Re* at the tube inlet. For SCO₂, the *f*/*f*₀, *Nu*/*Nu*₀ and *ψ* curves exhibit a sharp change across the pseudocritical point (*T*_c = 34.5 °C). Both the *Nu*/*Nu*₀ and *ψ* curves are in the maximum at the point, then level off quickly with increasing or decreasing *T*_b. There is the best HTE near the pseudocritical point for the TTIs based on *ψ* values. The HTE in the left-hand side of the point is better than the right-hand side of the point at *G* = 200 kg/

m²s. This situation, however, is reversed at *G* = 400 kg/m²s. The TTI with TR = 2.17 results in the highest *f*/*f*₀, *Nu*/*Nu*₀ and *ψ* at *G* = 200 kg/m²s. The TTIs with TR = 3.78, 5.39 are better than the TTI with TR = 2.17 in terms of *Nu*/*Nu*₀ and *ψ* at *G* = 400 kg/m²s. This fact implies that the TTI with TR = 2.17 is more likely suitable to a low SCO₂ mass flux, while the TTIs with TR = 3.78, 5.39 are more suitable to a high mass flux.

In Fig. 6(d)–(f), the *f*/*f*₀, *Nu*/*Nu*₀ and *ψ* curves are illustrated as a function of Reynolds number *Re* at the tube inlet and compared with similar experimental data using water and air. The higher the inlet temperature *T*₁, the larger the mean bulk temperature *T*_b, and the greater the Reynolds number *Re*. The more the mass flux, the higher the Reynolds number *Re* as well. When *Re* varies in the range of 6000–19,000, *f*/*f*₀ = 4.45–8.50 (far left of *T*_c), 3.63–7.29 (at *T*_c), 3.15–7.07 (far right of *T*_c), *Nu*/*Nu*₀ = 1.56–3.51 (far left of *T*_c), 3.43–5.75 (at *T*_c), 1.68–2.05 (far right of *T*_c), and *ψ* = 0.95–1.64 (far left of *T*_c), 1.90–2.94 (at *T*_c), 0.94–1.17 (far right of *T*_c) are held. The predicted *f*/*f*₀ curves of SCO₂ are similar to those of air and water, but above the experimental curves of them. The Λ-shaped *Nu*/*Nu*₀ and *ψ* curves are demonstrated, but the curves at *G* = 400 kg/m²s move to the region with high *Re*, and the *Nu*/*Nu*₀ and *ψ* values are lowered in comparison with the curves at *G* = 200 kg/m²s. This means that the effect of TTI on HTE gets weakened with increasing *Re*. This feature is the same as that in the thermal performance of TTI in convective heat transfer of air and water. Except in the region near the pseudocritical point, the predicted *Nu*/*Nu*₀ and *ψ* values of SCO₂ are comparable to the experimental data of air and water, the predicted *f*/*f*₀ values are all larger than the experimental data of air and water at TR = 2.17, 3.78, 5.39. There is an operational condition (*T*_b ≤ 33 °C or *T*₁ ≤ 34 °C) where the PEC is *ψ* < 1 at *G* = 400 kg/m²s. Although the TTI can enhance heat transfer under the condition of *ψ* < 1, this enhancement is not economical, and should not be recommended.

3.1.2. Effects of SCO₂ inlet pressure

The friction factor ratio *f*/*f*₀, Nusselt number ratio *Nu*/*Nu*₀, and PEC *ψ* in two inlet pressures *p*₁ = 8, 9 MPa, wall heat flux *q*_w = 12 kW/m² and mass flux *G* = 400 kg/m²s are demonstrated as a function of SCO₂ mean bulk temperature *T*_b and Reynolds number at the tube inlet *Re* in Fig. 7. Likewise, the *f*/*f*₀ curve against *T*_b has a jump across each the pseudocritical point, while the *Nu*/*Nu*₀, and *ψ* curves are in the peaks at two

Table 3

The information on the meshes in the fluid domain of the HX with TTI.

Sole tube geometrical model		with TTI			without TTI	
TR		2.17	3.78	5.39	Mesh2	
Element size(mm)		0.45	0.45	0.4	0.45	
Nodes		2,065,363	2,004,005	2,400,712	1,948,034	
Elements	Total	5,411,115	5,234,579	6,231,617	5,096,858	
	Pyr5	109,650(2%)	97,537(2%)	100,840(2%)	96,079(2%)	
	Tet4	2,171,031(40%)	206,226(36%)	206,226(39%)	2,038,438(40%)	
	Wed6	3,130,434(58%)	3,597,046(62%)	3,597,046(59%)	2,962,431(58%)	
Element quality		0.3671 ± 0.3610	0.3651 ± 0.3611	0.3512 ± 0.3722	0.3645 ± 0.3712	
Aspect ratio		22.72 ± 26.80	22.99 ± 28.84	28.42 ± 34.18	23.74 ± 26.29	
Skewness		0.2365 ± 0.2141	0.2347 ± 0.2121	0.2418 ± 0.2204	0.2188 ± 0.2121	
Orthogonal quality		0.7473 ± 0.2296	0.7498 ± 0.2271	0.7390 ± 0.2422	0.7607 ± 0.2320	
Inflation mesh for boundary layer	First layer height (mm)	tube	0.005	0.004	0.005	0.004
		TTI	0.0055	0.0055	0.004	0.0055
		Number of layers	tube	14	14	14
	TTI	16	16	16	16	
	Growth rate	1.2	1.2	1.2	1.2	
<i>y</i> ⁺	<i>G</i> = 400 kg/m ² s <i>q</i> _w = 12 kW/m ² <i>p</i> ₁ = 8 MPa <i>T</i> ₁ = 26–60°C	2.43–6.20	2.23–6.03	1.79–4.86	2.19–5.90	0.86–2.67

Pyr5-five-node pyramid element, Tet4-four-node tetrahedron element, We6-six-node wedge element, *y*⁺ = √(τ_w/ρ*y*_n)/ν, where τ_w is the shear stress at the wall, *y*_n is the distance to the nearest wall and ν is the local kinematic viscosity of SCO₂; *y*⁺ rises with increasing *T*₁.

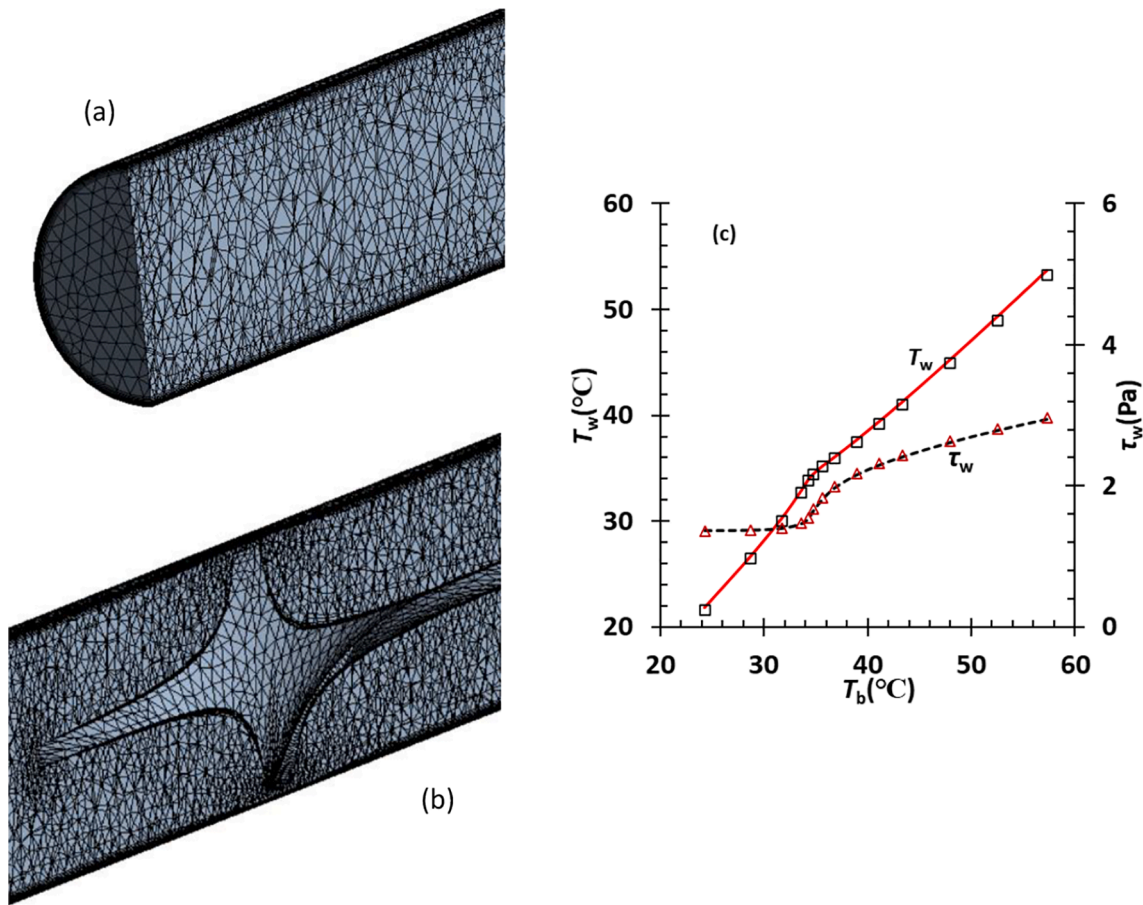


Fig. 4. The close-up of the mesh in fluid domain of the HX with TTI and SCO_2 mean shear stress and temperature at the tube wall, (a) the mesh near the tube inlet, (b) the mesh near the TTI inlet, (c) mean wall temperature T_w and mean wall shear stress at the tube wall in the fair mesh (line) and fine mesh (symbol).

pseudocritical points ($T_c = 34.5^\circ\text{C}$ in $p_1 = 8\text{ MPa}$, $T_c = 40^\circ\text{C}$ in $p_1 = 9\text{ MPa}$). The peak SCO_2 specific heat capacity at the pseudocritical point and $p_1 = 9\text{ MPa}$ is 12.8 kJ/kg K compared with 35.2 kJ/kg K at the pseudocritical point ($T_c = 34.5^\circ\text{C}$) in $p_1 = 8\text{ MPa}$, i.e., the former is 63.6% smaller than the latter. Further, the SCO_2 specific heat capacity curve in $p_1 = 9\text{ MPa}$ varies with temperature less significantly than the curve in $p_1 = 8\text{ MPa}$. Therefore, Nu/Nu_0 , and ψ curves in $p_1 = 9\text{ MPa}$ are flatter than those in $p_1 = 8\text{ MPa}$ but also have lower Nu/Nu_0 , and ψ peak values than the latter. For the TTIs with $\text{TR} = 2.17, 3.78, 5.39$, their ψ curves are greater than 1 in $p_1 = 9\text{ MPa}$. The TTI with $\text{TR} = 3.78$ is more suitable to the $p_1 = 9\text{ MPa}$ operational condition.

When the SCO_2 mass flux, inlet temperature and tube diameter are given, the Reynolds number in $p_1 = 9\text{ MPa}$ is smaller than the number in $p_1 = 8\text{ MPa}$ due to increased SCO_2 density and less variation of dynamic viscosity. As a result, the f/f_0 , Nu/Nu_0 , and ψ curves in $p_1 = 9\text{ MPa}$ shift to the left of the curves in $p_1 = 8\text{ MPa}$. When the inlet pressure increases to 9 MPa from 8 MPa , $f/f_0 = 4.45\text{--}11.00$ (far left of T_c), $4.15\text{--}8.34$ (at T_c), $3.15\text{--}7.14$ (far right of T_c), $Nu/Nu_0 = 1.56\text{--}3.00$ (far left of T_c), $3.86\text{--}3.54$ (at T_c), $1.68\text{--}2.05$ (far right of T_c), and $\psi = 0.95\text{--}1.37$ (far left of T_c), $2.24\text{--}1.79$ (at T_c), $0.94\text{--}1.28$ (far right of T_c) persist. The predicted f/f_0 values are much larger than the f/f_0 experimental data of water and air, but also show a sharper slope against decreasing Re than the latter. The estimated Nu/Nu_0 , and ψ values are comparable to the counterparts of water and air, especially for the case of $p_1 = 9\text{ MPa}$. This fact suggests the Nu/Nu_0 , and ψ curves will approach to those of water and air gradually when the SCO_2 inlet pressure increases steadily.

3.1.3. Effects of wall heat flux

The friction factor ratio f/f_0 , Nusselt number ratio Nu/Nu_0 , and PEC

ψ in two wall heat fluxes $q_w = 12, 24\text{ kW/m}^2$, inlet pressures $p_1 = 8\text{ MPa}$ and mass flux $G = 200\text{ kg/m}^2\text{s}$ are illustrated as a function of SCO_2 mean bulk temperature T_b and Reynolds number at the tube inlet Re in Fig. 8. When the SCO_2 mass flux and inlet pressure are given, the wall heat flux can alter the SCO_2 mean HTC but not the Reynolds number Re . Thus, the f/f_0 , Nu/Nu_0 , and ψ curves in $q_w = 12\text{ kW/m}^2$ don't shift relatively to those in $q_w = 24\text{ kW/m}^2$ in the abscissa direction but can move in the ordinate direction. The TTIs in $q_w = 24\text{ kW/m}^2$ performs better than in $q_w = 12\text{ kW/m}^2$. When Re is in the range of $6000\text{--}19000$, $f/f_0 = 4.64\text{--}10.85$ (far left of T_c), $4.15\text{--}8.71$ (at T_c), $4.01\text{--}8.19$ (far right of T_c), $Nu/Nu_0 = 2.73\text{--}4.48$ (far left of T_c), $3.93\text{--}6.93$ (at T_c), $1.76\text{--}1.96$ (far right of T_c), and $\psi = 1.64\text{--}2.02$ (far left of T_c), $2.83\text{--}3.33$ (at T_c), $1.06\text{--}1.13$ (far right of T_c) yield. The numerical values of f/f_0 are considerably higher than the experimental data of water and air. The predicted Nu/Nu_0 and ψ values are essentially in line with the experimental Nu/Nu_0 and ψ values of water and air. The Nu/Nu_0 and ψ curves drop off quickly in the right-hand side of the pseudocritical point. In the given mass flux, inlet pressure and wall heat flux, the condition $\psi \geq 1$ is held, and TR has the largest influence on ψ when TR values are ranged in 2.17 and 3.78.

3.1.4. Optimal TR

When the optimal TR is determined, the f/f_0 and ψ should be considered together. The $\psi/f/f_0$ curves are present in Fig. 9 in various mass fluxes, inlet pressures and wall heat fluxes. In the experiment data [44,55], the maximum f/f_0 is smaller than 5. Therefore, $f/f_0 \leq 5$ is adopted as the criterion for determining the optimal TR in terms of ψ . Based on Fig. 9, $\text{TR} = 3.78$ appears to be the optimal TR under the operational condition of $G = 200\text{ kg/m}^2\text{s}$, $p_1 = 8\text{ MPa}$ and $q_w = 12\text{ kW/}$

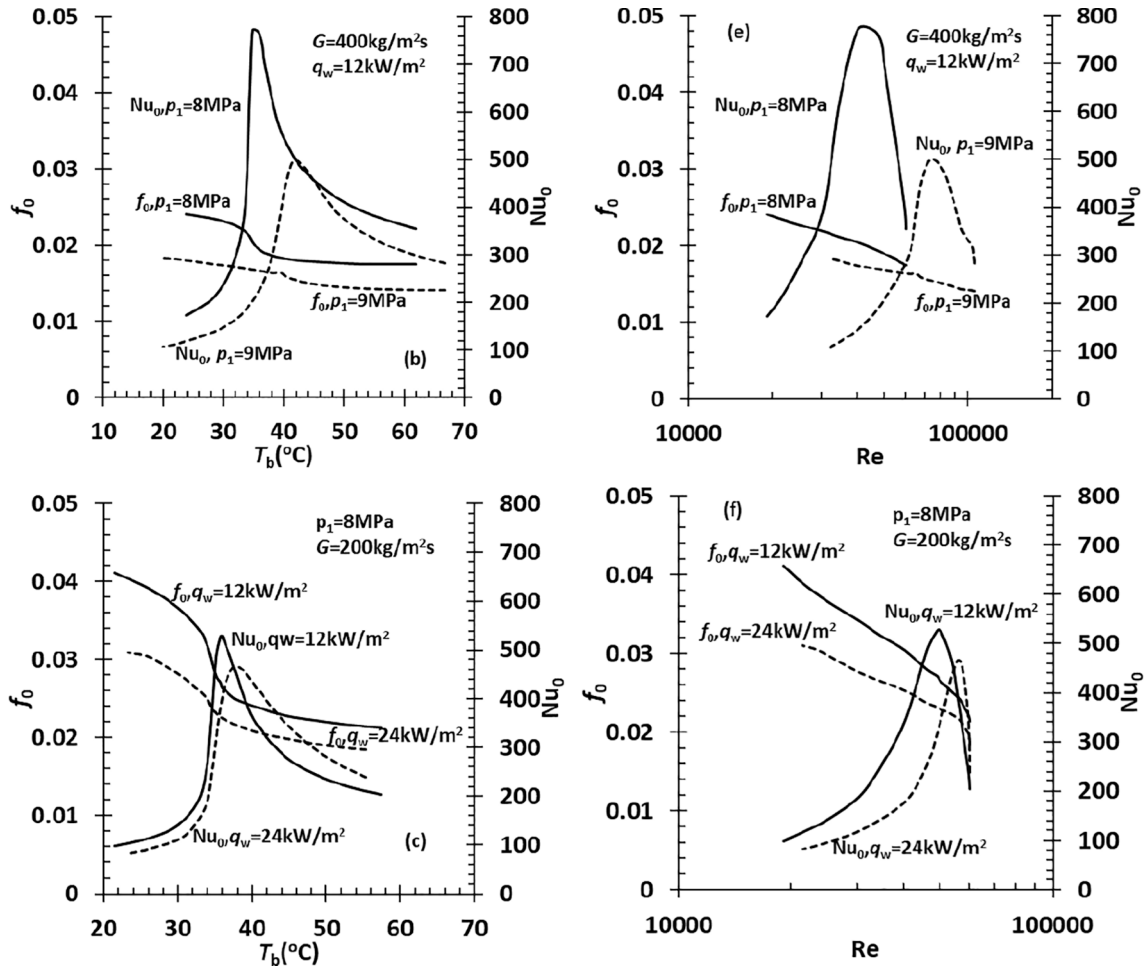


Fig. 5. The friction factor f_0 and Nusselt number Nu_0 in the HX without TTI in two mass fluxes, inlet pressures and wall heat fluxes, respectively, (a)–(c) as a function of mean bulk temperature T_b , (d)–(f) as a function of Reynolds number at the tube inlet Re.

m^2 ; whilst $TR = 5.39$ should be the optimal value under the condition of $G = 400 \text{ kg/m}^2\text{s}$, $p_1 = 8, 9 \text{ MPa}$ and $q_w = 12 \text{ kW/m}^2$ or $G = 200 \text{ kg/m}^2\text{s}$, $p_1 = 8 \text{ MPa}$ and $q_w = 24 \text{ kW/m}^2$. Clearly, those optimal TR values need to be confirmed by experiment late on in our laboratory.

3.2. Characterisation of thermal performance of TTI

The TTI is the key element for HTE in an HX, but how to characterise the thermal performance of a TTI is an important but neglected issue in the literature. Here the thermal performance of a TTI is referred to as a relationship between a fluid dynamic parameter and the HTC in the HX with TTI. The relationship will reflect the HTE caused by TTIs. A TTI results in a fluid element into the rotation to form a vortex around the axis of the TTI or a streamline itself as soon as the fluid enters the TTI, as shown in Fig. 10. Additionally, the thermal and fluid parameters of SCO_2 vary not only in both the radial and the circumferential directions but also in the axial direction, see Fig. 11. To simplify the characterisation of thermal performance of TTI, the radial and circumferential average, i.e., cross-sectional average thermal and fluid parameters in the inlet and outlet of the TTI and ten cross-sections equally distributed along the axis of the TTI, as illustrated in Fig. 11, are extracted and analysed.

The absolute helicity H and vorticity (velocity curl) Ω can potentially be employed as the parameters to determine vortex shape or region in a TTI. The absolute helicity H is the absolute value of the dot product of the velocity vector and vorticity vector of fluid. The vorticity Ω is the magnitude of the vorticity vector of fluid. The mathematic expressions of the two parameters are present in Appendix B and their details can be

found in [60,61]. As an example, the vortex regions identified by using the absolute helicity H and vorticity Ω are illustrated in Fig. 12 under the conditions: $TR = 3.78$, $G = 200 \text{ kg/m}^2\text{s}$, $p_1 = 8 \text{ MPa}$, $T_1 = 45 \text{ }^\circ\text{C}$, $q_w = 24 \text{ kW/m}^2$ based on the thresholds: $H = 165$, 1646 m/s^2 , $\Omega = 474$, $18,956 \text{ s}^{-1}$, respectively. The vortex regions identified by the small thresholds are in the channel of the TTI, while the regions determined by the large thresholds mainly accumulate on the surfaces of the TTI and in the corners between the TTI and the tube wall. Notably, the vortex regions given by the two parameters are similar in shape. The vortex regions identified by the vorticity are more extensively concentrated in the boundary layer where the highest vorticity is generated by the shearing effect. The vortex regions given by the absolute helicity have a little effect caused by the boundary layer and more likely reflect the rotation of fluid, because $H = 0$ is held theoretically at the wall. The shapes of the vortex regions determined with reduced absolute helicity and vorticity thresholds at low inlet temperatures are similar to the shapes at $T_1 = 45 \text{ }^\circ\text{C}$, thus are no longer illustrated.

The local Nusselt number contours on the insert and tube wall are illustrated in Fig. 13, where the local Nusselt number has defined the ratio of the product of the local wall HTC and tube inner diameter to the local thermal conductivity of SCO_2 under the conditions such as $TR = 3.78$, $G = 200 \text{ kg/m}^2\text{s}$, $p_1 = 8 \text{ MPa}$, $T_1 = 32, 36, 45 \text{ }^\circ\text{C}$, and $q_w = 24 \text{ kW/m}^2$. The local wall HTC is calculated by the local wall heat flux divided by the difference between local wall adjacent temperature and local wall temperature. The higher local Nusselt number is found near the circumferential tip and the lower number is located in the central area on the tape surface. Similarly, the higher local Nusselt number on the

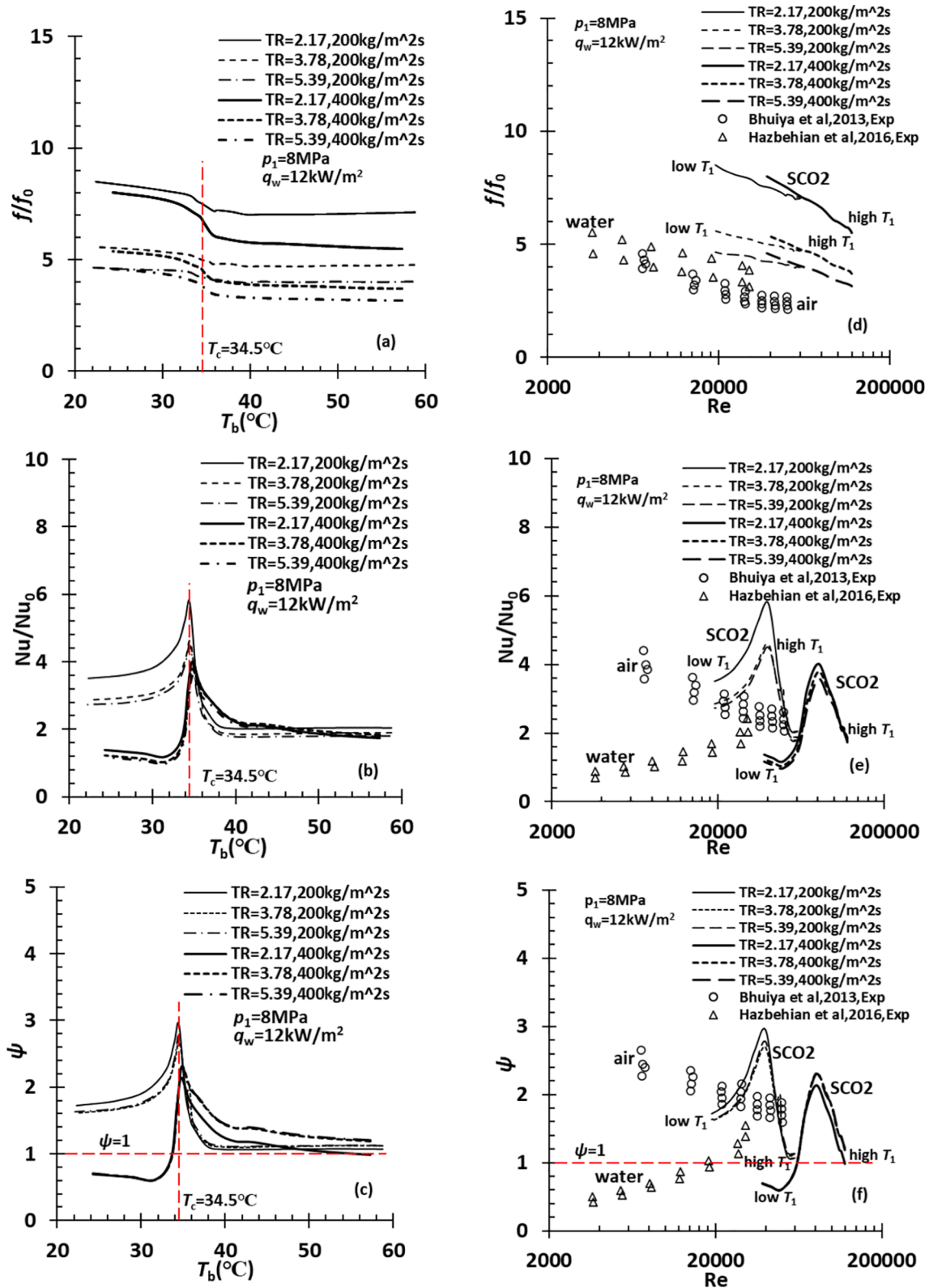


Fig. 6. The friction factor f/f_0 , Nusselt number ratio Nu/Nu_0 , and PEC ψ curves of the HXs with TTI in two mass fluxes of $G = 200, 400 \text{ kg/m}^2\text{s}$, (a)–(c) plotted as a function of CO_2 mean bulk temperature T_b , (d)–(f) plotted as a function of Reynolds number at the tube inlet Re , the experimental data of Bhuiya et al. (2013) for air are adapted from [44], the data of Hazbehan et al. (2016) for water are from [55].

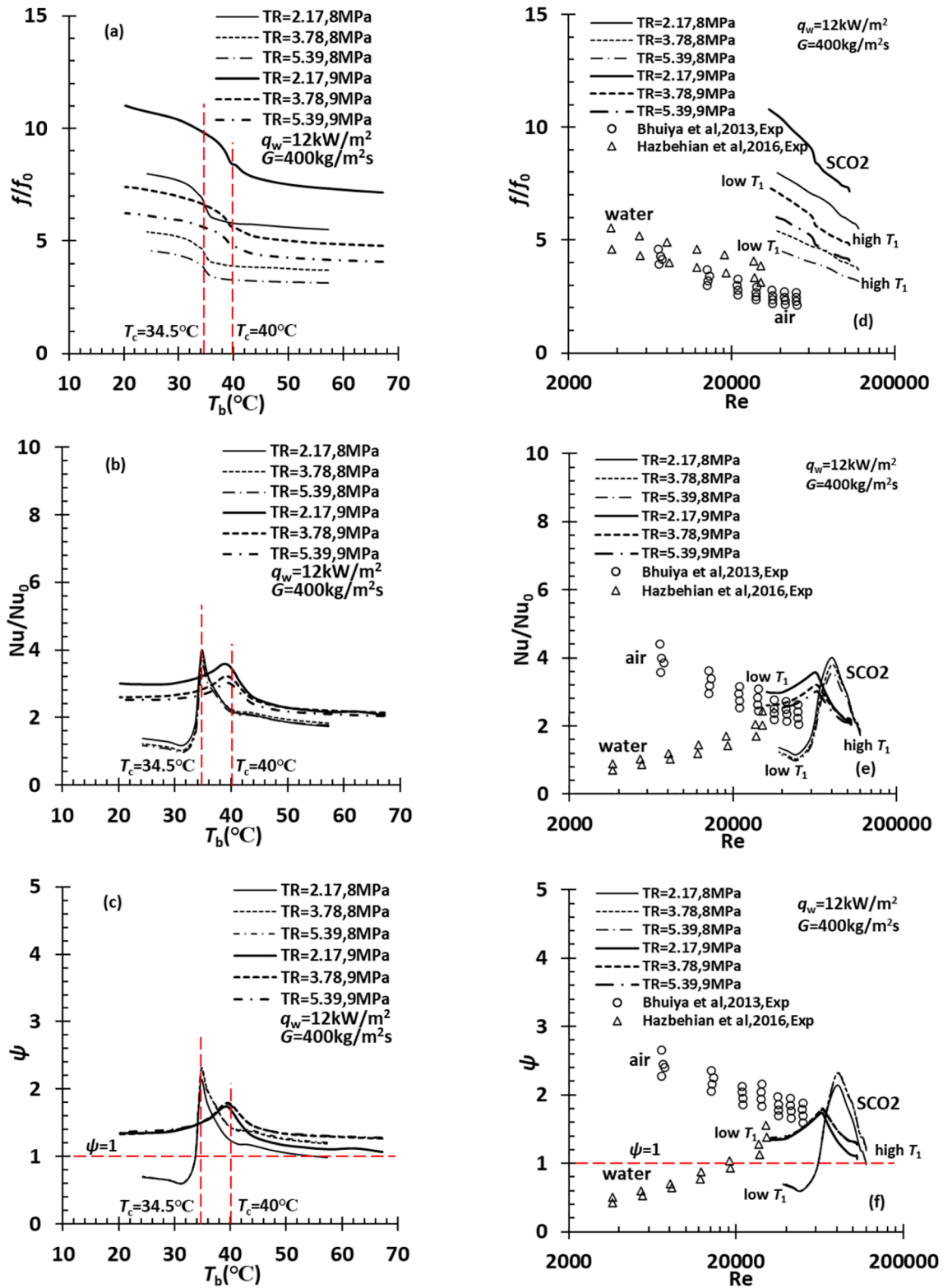


Fig. 7. The friction factor ratio f/f_0 , Nusselt number ratio Nu/Nu_0 , and PEC ψ curves of the HXs with TTI in two SCO_2 inlet pressures of $p_1 = 8, 9$ MPa, (a)–(c) plotted as a function of SCO_2 mean bulk temperature T_b , (d)–(f) plotted as a function of Reynolds number at the tube inlet Re , the experimental data of Bhuiya et al. (2013) for air are adapted from [44], the data of Hazbehan et al. (2016) for water are from [55].

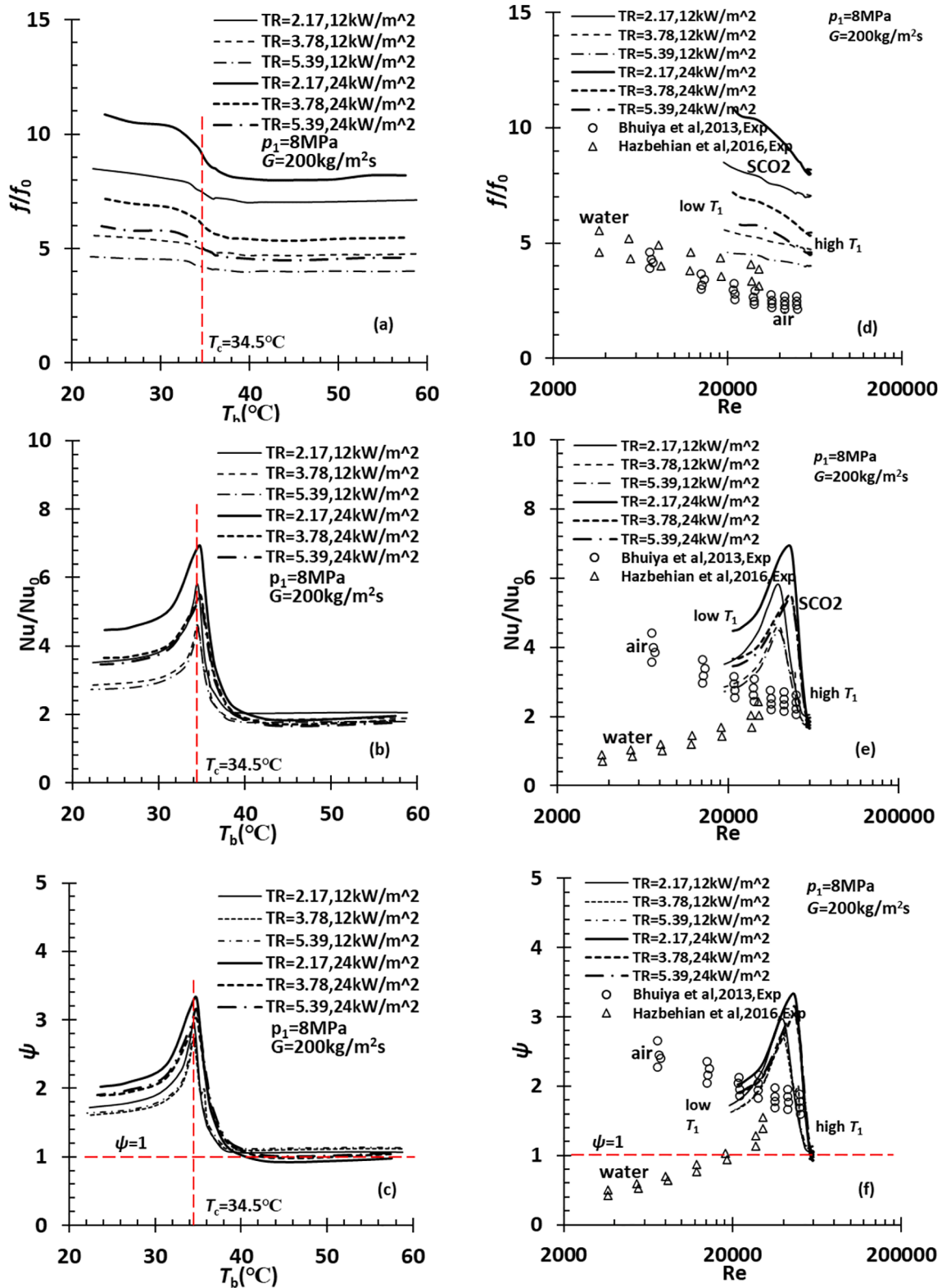


Fig. 8. The friction factor ratio f/f_0 , Nusselt number ratio Nu/Nu_0 , and PEC ψ curves of the HX with TTI in two wall heat fluxes of $q_w = 12, 24 \text{ kW/m}^2$ caused by cold water, (a)–(c) plotted as a function of SCO₂ bulk temperature T_b , (d)–(f) plotted as a function of Reynolds number at the tube inlet Re , the experimental data of Bhuiya et al. (2013) for air are adapted from [44], the data of Hazbehan et al. (2016) for water are from [55].

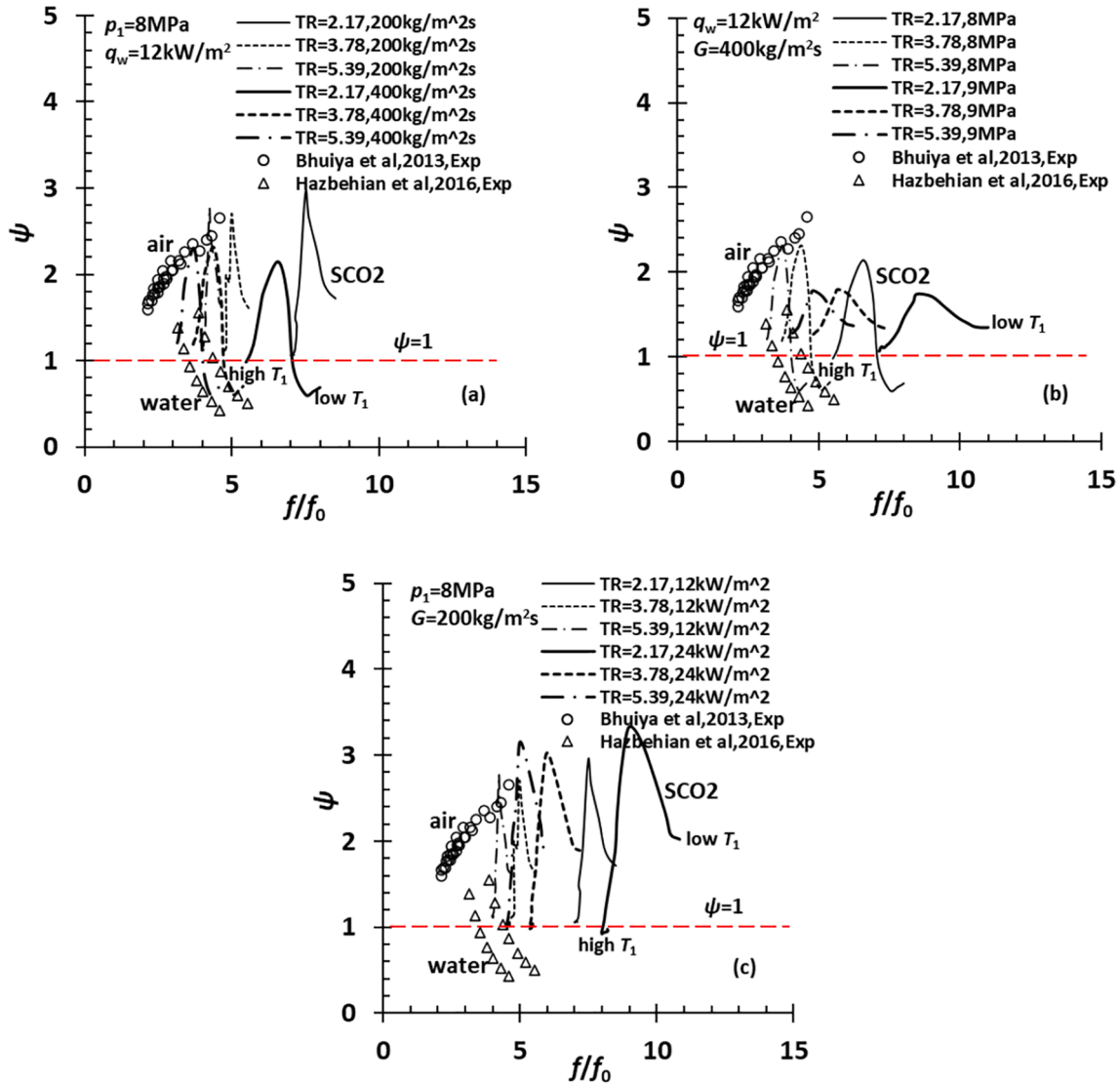


Fig. 9. The PEC ψ curves in terms of friction factor ratio f/f_0 under two different SCO_2 mass flux, inlet pressure and wall heat flux conditions, (a) variable mass flux G , (b) variable inlet pressure p_1 , (c) variable wall heat flux q_w .

tube wall is accumulated in the areas near the insert tip, while the lower Nusselt number is identified on the tube wall far off the insert tip. Compared with Fig. 12, the areas with a higher local Nusselt number coincide with the areas in a larger absolute helicity and vorticity of SCO_2 . This fact suggests that the vortex kinetics should play a role in the HTE induced by a TTI.

The cross-sectional mean absolute helicity H_b is plotted against the cross-sectional mean velocity curl Ω_b in Fig. 14 for three cases. Essentially, H_b rises with increasing Ω_b , especially, H_b can be correlated with Ω_b at a given inlet temperature. In this context, we can make use of either one of them to identify the vortex region and characterise the thermal performance of a TTI. Since the cross-sectional mean absolute helicity H_b represents the rotation of fluid in a more extensive degree than the mean velocity curl Ω_b does, H_b is adopted here.

To demonstrate if the cross-sectional mean absolute helicity H_b can

reflect the influence caused by the change in SCO_2 mass flux, inlet pressure, wall heat flux and TR, the $H_b/H_{b1}-z/l$ and $U_{wb}-H_b$ curves under the conditions of variable SCO_2 mass flux, inlet pressure, wall heat flux and TR are composed and demonstrated in Fig. 15, respectively, where H_{b1} is the mean absolute helicity at the TTI entrance. U_{wb} is the mean wall HTC of ten cross-sections shown in Fig. 11. The individual wall HTC U_w for calculating U_{wb} is estimated in CFX-Post by using the following formula [62].

$$U_w = \frac{q_w}{T_{nw} - T_w} \quad (3)$$

where T_{nw} is wall adjacent temperature, which is the average temperature in the element adjacent to the wall, T_w is wall temperature, which is calculated from the thermal wall function expressed with Eq. (A.13) in Appendix A.

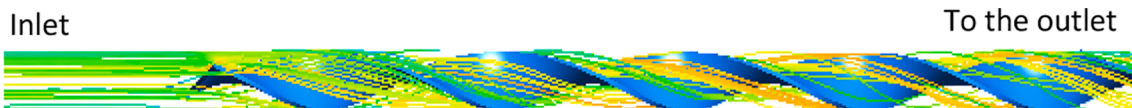


Fig. 10. The streamlines of SCO_2 flowing in the HX with a TTI under the conditions: $\text{TR} = 3.78$, $G=200 \text{ kg/m}^2\text{s}$, $p_1=8 \text{ MPa}$, $T_1=45 \text{ }^\circ\text{C}$, $q_w=24 \text{ kW/m}^2$.

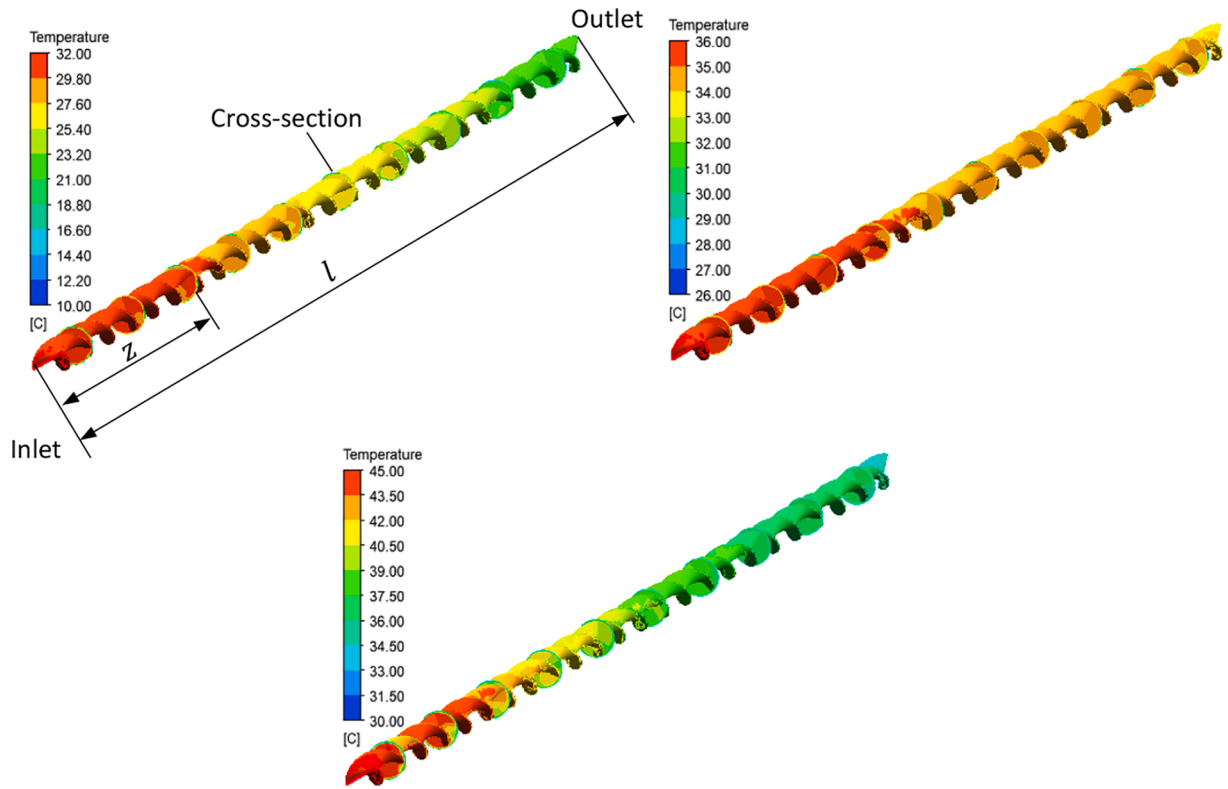


Fig. 11. The SCO_2 temperature contours on the surface of the TTI and in the ten cross-sections equally distributed (50 mm gap) across the tube under the conditions: $\text{TR} = 3.78$, $G=200 \text{ kg/m}^2\text{s}$, $p_1=8 \text{ MPa}$, $T_1=45, 36, 32 \text{ }^\circ\text{C}$, $q_w=24 \text{ kW/m}^2$.

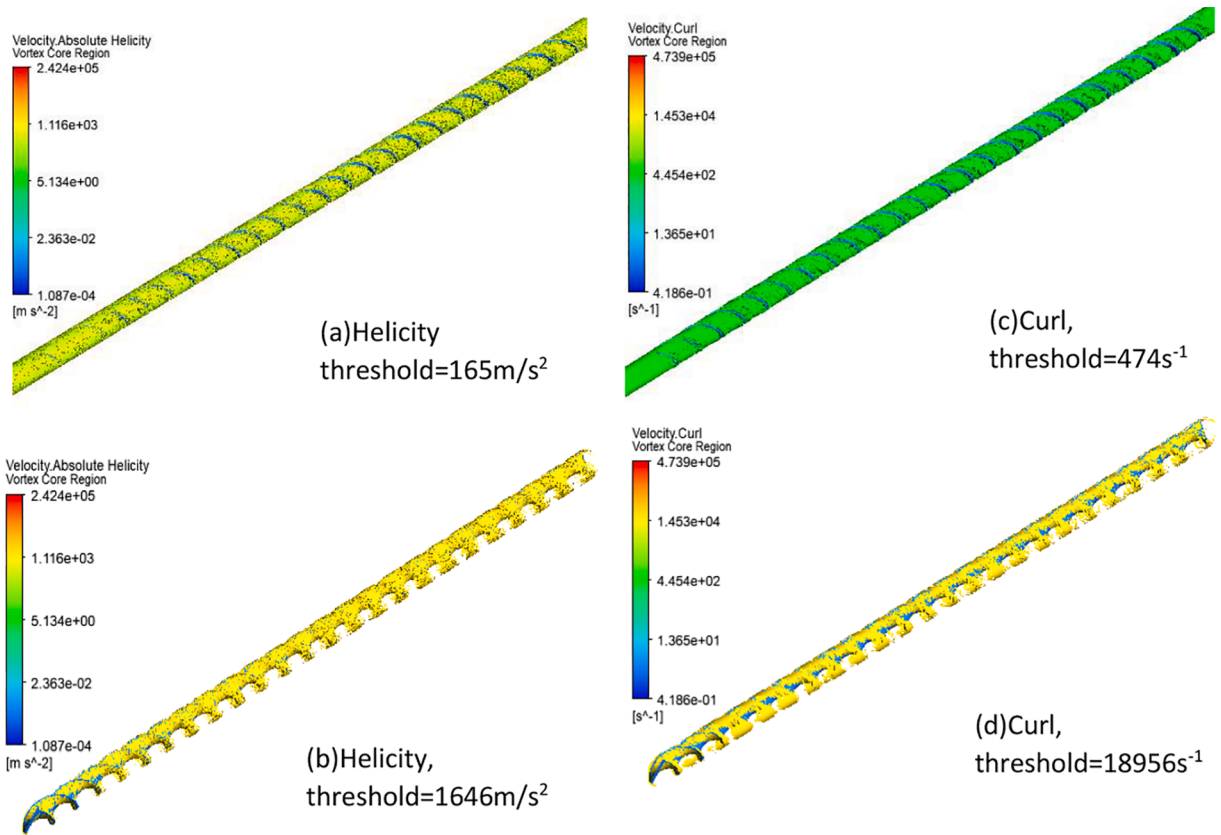


Fig. 12. The vortex region determined by the absolute helicity H and velocity curl Ω , respectively, (a) and (b) the vortex region by the helicity H , (c) and (d) the vortex region by the curl Ω , under the conditions: $\text{TR} = 3.78$, $G=200 \text{ kg/m}^2\text{s}$, $p_1=8 \text{ MPa}$, $T_1=45 \text{ }^\circ\text{C}$, and $q_w = 24 \text{ kW/m}^2$.

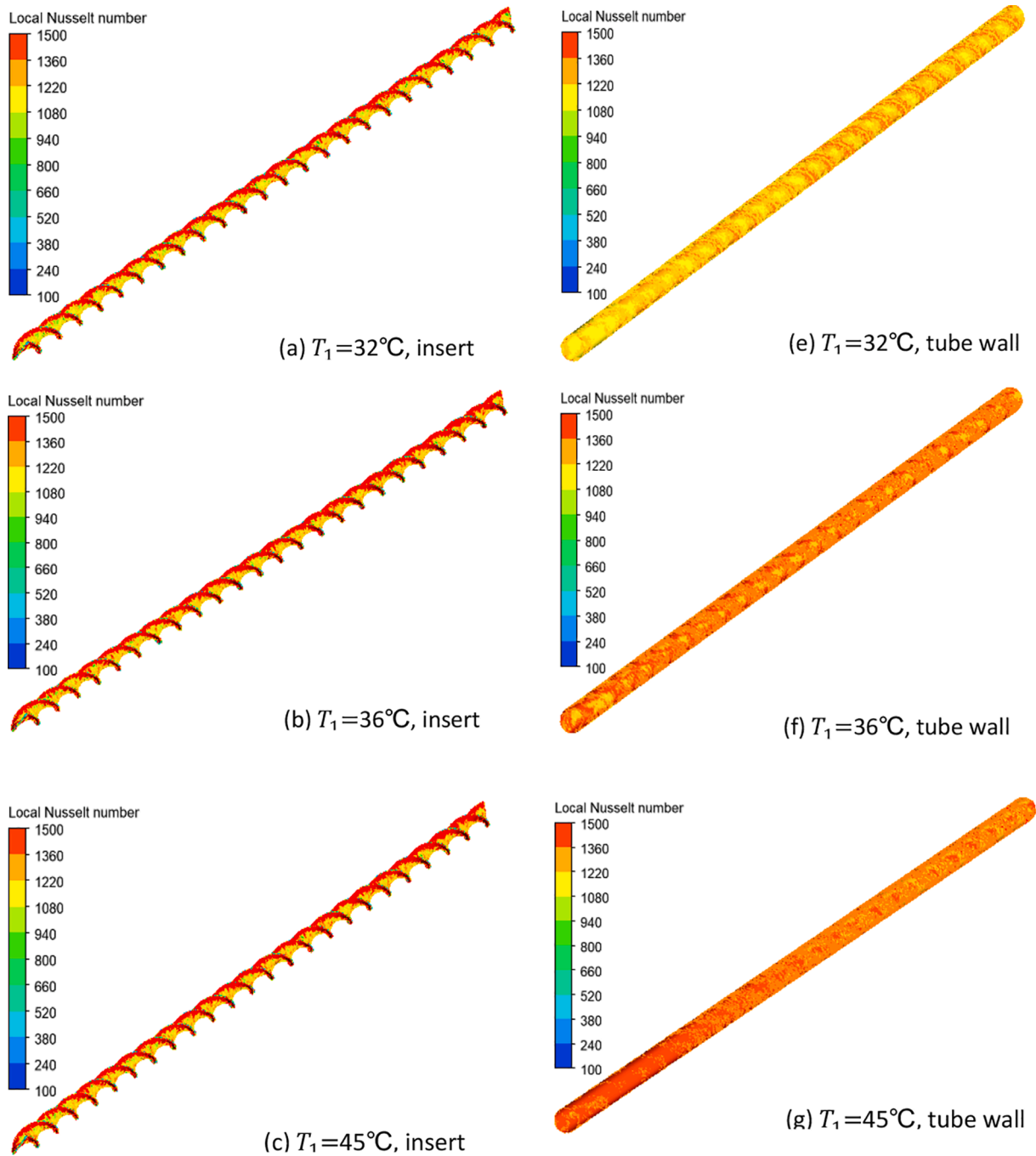


Fig. 13. The local Nusselt number contours on the insert and tube wall, the number is defined the ratio of the product of local wall heat transfer coefficient and tube inner diameter to the local thermal conductivity of SCO_2 under the conditions: $\text{TR} = 3.78$, $G = 200 \text{ kg/m}^2\text{s}$, $p_1 = 8 \text{ MPa}$, $T_1 = 32, 36, 45 \text{ }^\circ\text{C}$, and $q_w = 24 \text{ kW/m}^2$, the local wall heat transfer coefficient is calculated by the local wall heat flux divided by the difference between local wall adjacent temperature and local wall temperature.

In Fig. 15(a), the parameter H_b/H_{b1} rises rapidly in the range $z/l = 0-0.2$ after SCO_2 enters the TTI, then experiences a slight increase until $z/l = 0.8$, and levels off toward the outlet. Thus, the mechanism of HTE by a TTI may be associated with absolute helicity. In Fig. 15(b), the cross-sectional mean wall HTC U_{wb} can be correlated linearly with the cross-sectional mean absolute helicity H_b . The U_{wb} value determined by the linear correlation and its slope connect with the HTE generated by the TTI. Specially, the higher the U_{wb} value, the better the HTE; the larger slope, the more sensitive the U_{wb} in response to the change in the absolute helicity of the vortex generated by the TTI, and eventually the more efficient the HTE. Based on Fig. 6 the thermal performance of the

TTI with $\text{TR} = 3.78$ in $G = 200 \text{ kg/m}^2\text{s}$ is better than in $G = 400 \text{ kg/m}^2\text{s}$. The U_{wb} value and its slope in terms of H_b in $G = 200 \text{ kg/m}^2\text{s}$ are consistently larger than those in $G = 400 \text{ kg/m}^2\text{s}$ at a given inlet temperature.

In Fig. 15(c), the H_b/H_{b1} curves at $T_1 = 45, 36$ (near the pseudocritical point), $30 \text{ }^\circ\text{C}$ in $p_1 = 8 \text{ MPa}$ inlet pressure are below the curves at $T_1 = 45, 41$ (near the pseudocritical point), $30 \text{ }^\circ\text{C}$ in $p_1 = 9 \text{ MPa}$ inlet pressure, but also H_b/H_{b1} increases along the axis of TTI in the former faster than in the latter. The slopes of the corresponding $U_{wb}-H_b$ correlations in the former are steeper than in the latter, as shown in Fig. 15(d). Except near the pseudocritical point, the U_{wb} values in $p_1 = 8 \text{ MPa}$ inlet

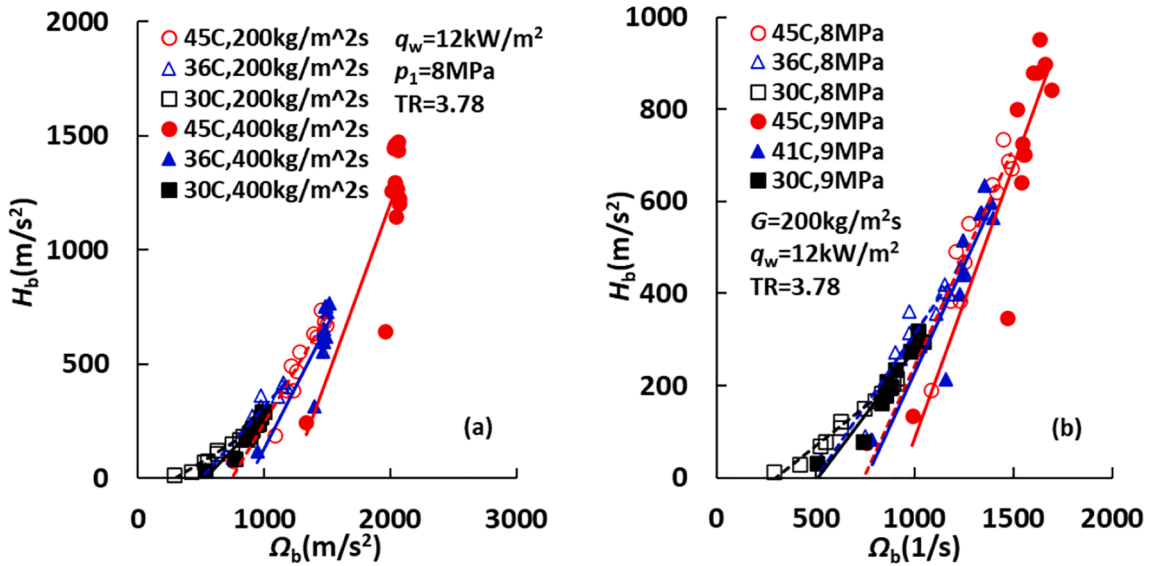


Fig. 14. The cross-sectional mean absolute helicity H_b versus the cross-sectional velocity curl Ω_b for three cases, (a) $TR = 3.78$, $G = 200, 400 \text{ kg/m}^2\text{s}$, $p_1 = 8 \text{ MPa}$, $T_1 = 45, 36, 30 \text{ }^\circ\text{C}$, $q_w = 12 \text{ kW/m}^2$ (b) $TR = 3.78$, $G = 200 \text{ kg/m}^2\text{s}$, $p_1 = 8, 9 \text{ MPa}$, $T_1 = 45, 41, 30 \text{ }^\circ\text{C}$, and $q_w = 12 \text{ kW/m}^2$.

pressure are smaller than the values in $p_1 = 9 \text{ MPa}$ inlet pressure. This suggests that the thermal performance of the TTI in $p_1 = 8 \text{ MPa}$ inlet pressure is better near the pseudocritical point but poorer on both the left- and right-hand sides of the point. This situation is coincident with that presented in Fig. 7.

In Fig. 15(e), the H_b/H_{b1} curve in $q_w = 12 \text{ kW/m}^2$ wall heat flux is similar to the curve in $q_w = 24 \text{ kW/m}^2$ wall heat flux at $T_1 = 45, 36, 30 \text{ }^\circ\text{C}$, but slightly higher than the latter. The slopes of the $U_{wb}-H_b$ correlations in $q_w = 12 \text{ kW/m}^2$ are a little flatter than in $q_w = 24 \text{ kW/m}^2$, and the U_{wb} values are lower than in the latter at the three inlet temperatures, as demonstrated in Fig. 15(f). This means that the thermal performance of the TTI in $q_w = 24 \text{ kW/m}^2$ is better than in $q_w = 12 \text{ kW/m}^2$. This outcome agrees with that in Fig. 8.

In Fig. 15(g), the H_b/H_{b1} curves at $TR = 2.17$ are all above the curves at $TR = 3.78$ at $T_1 = 45, 36, 30 \text{ }^\circ\text{C}$, and increase quicker and higher than the latter, suggesting the stronger absolute helicity at $TR = 2.17$. The slopes of the $U_{wb}-H_b$ correlations at $TR = 2.17$ are steeper than at $TR = 3.78$, especially at $T_1 = 36, 30 \text{ }^\circ\text{C}$. The U_{wb} values at $TR = 2.17$ are lower than the values at $TR = 3.78$ in most region of H_b . In the rest region (high H_b), however, the U_{wb} values at $TR = 2.17$ are larger than those at $TR = 3.78$, as indicated in Fig. 15(h). When the inlet temperatures are $T_1 = 36, 30 \text{ }^\circ\text{C}$, the mean U_{wb} across the H_b range at $TR = 2.17$ is slightly larger than the mean at $TR = 3.78$. When the inlet temperature is $T_1 = 45 \text{ }^\circ\text{C}$, the mean U_{wb} at $TR = 2.17$ is slightly smaller than the mean at $TR = 3.78$. Therefore, the thermal performance of the TTI at $TR = 2.17$ should be a little better than the performance at $TR = 3.78$. This result is comparable to that in Fig. 6.

4. Discussion

In the present article, three TTIs were designed for an experimental counter-flow tube-in-tube HX based on the information available about TTIs in the literature. Then, the convective heat transfer of SCO_2 was simulated based on the 3D RANS and SST flow models by using CFD method under variable conditions in TR , mass flux, inlet pressure, wall heat flux when the SCO_2 inlet temperature varies in a range. The optimal

TR s were determined based on the ψ curve and $f/f_0 \leq 5$ criterion. The thermal performance of the TTIs was characterised by means of cross-sectional average absolute helicity and wall HTC. It is the first time for TTIs being investigated under SCO_2 flow conditions and characterised by the cross-sectional average absolute helicity in the literature.

The swirling strength Y associated with the analysis of eigenvalues of velocity gradient tensor in Appendix B is often adopted to identify vortex regions in a flow field. To confirm if the swirling strength is applicable to the vortex in a TTI or not, the vortex region was determined with the strength at a threshold $Y = 396 \text{ s}^{-1}$, the $Y_b/Y_{b1}-z/l$ and $U_{wb}-Y_b$ curves were generated under the conditions: $TR = 3.78$, $G = 200, 400 \text{ kg/m}^2\text{s}$, $p_1 = 8 \text{ MPa}$, $T_1 = 45, 36, 30 \text{ }^\circ\text{C}$, and $q_w = 24 \text{ kW/m}^2$, as shown in Fig. 16, where Y_{b1} is the Y_b at the TTI inlet. It can be seen that the vortex region is located in the corners between the TTI and the tube wall, and at the tube wall with many spots. The swirling strength Y seems to be unable to exclude the vorticity in the boundary layer. The Y_b/Y_{b1} curves in $200 \text{ kg/m}^2\text{s}$ rise steadily along the tube after SCO_2 enters the TTI; in $400 \text{ kg/m}^2\text{s}$, however, the Y_b/Y_{b1} curves ascend quickly in the range of $z/l = 0-0.2$, then experience a slight increase until the exit. Furthermore, the Y_b/Y_{b1} curve at $T_1 = 45 \text{ }^\circ\text{C}$ overlaps the curve at $T_1 = 36 \text{ }^\circ\text{C}$. Based on Fig. 6 the thermal performance of the TTI with $TR = 3.78$ in $G = 200 \text{ kg/m}^2\text{s}$ is better than in $G = 400 \text{ kg/m}^2\text{s}$. Unfortunately, the U_{wb} value and its slope of the correlation between U_{wb} and Y_b in $G = 200 \text{ kg/m}^2\text{s}$ are not consistently superior to those in $G = 400 \text{ kg/m}^2\text{s}$. Considering the behaviour of the swirling strength Y in the vortex identification and the presentation of $Y_b/Y_{b1}-z/l$ and $U_{wb}-Y_b$ curves, the swirling strength Y might not be the best indicator for representing the thermal performance of a TTI.

According to Fig. 16, the TTI with a nearly linear $H_b/H_{b1}-z/l$ curve and larger slope as well as smaller H_b level corresponds to a better thermal performance in most cases. To achieve this goal, a variable pitch might be adopted. Nonetheless, an experimental validation of this finding is needed. The optimal level of absolute helicity needs to be determined for a given TTI under various operational conditions or for a given operational condition in various geometries of a TTI in the future.

Note that there are a few limitations to this paper. First, there is no

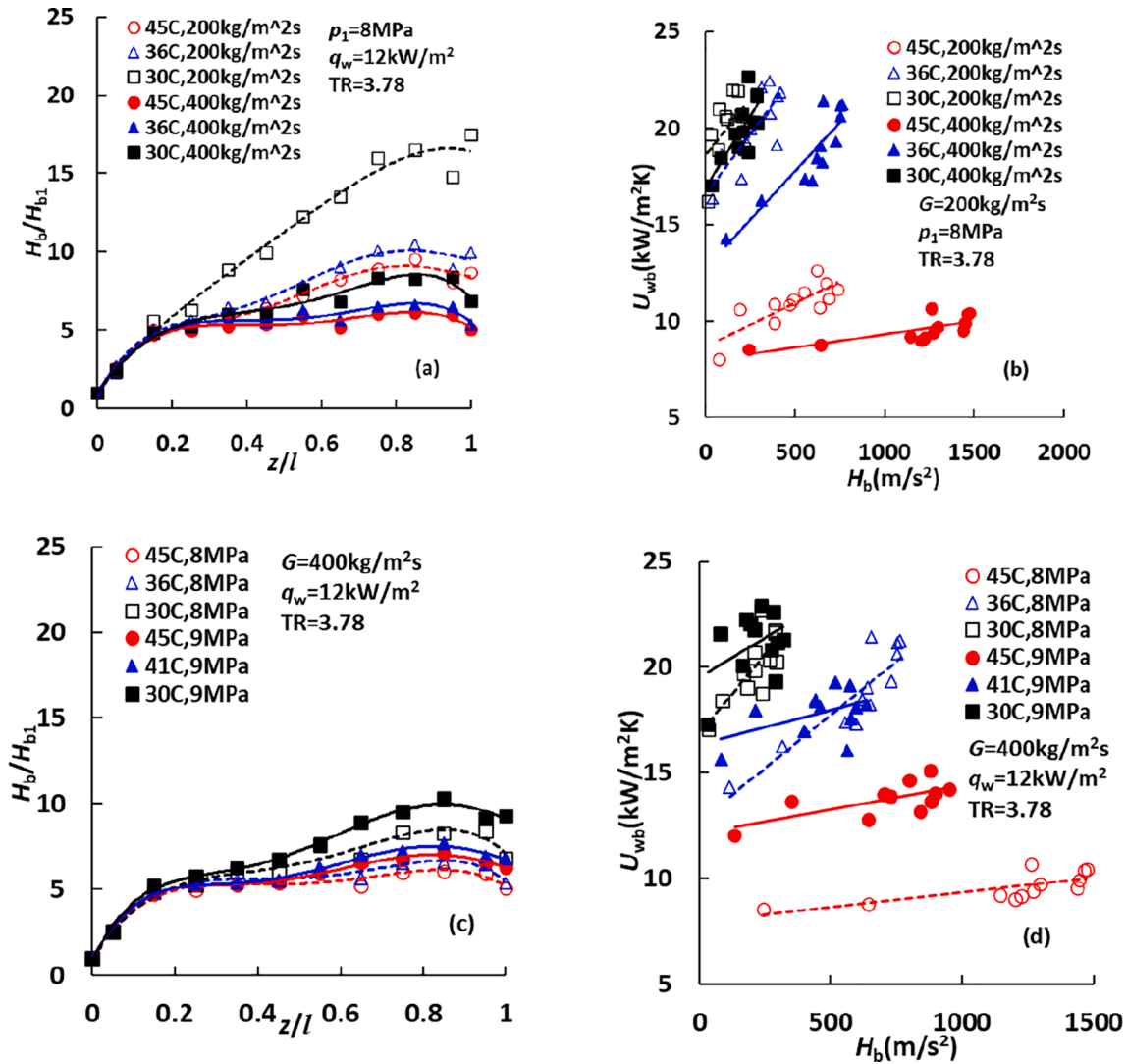


Fig. 15. The dimensionless cross-sectional mean absolute helicity H_b/H_{b1} as a function of dimensionless axial coordinate z/l , and the cross-sectional mean wall heat transfer coefficient U_{wb} curves are against the cross-sectional mean absolute helicity H_b , (a) and (b) under the conditions: $TR = 3.78$, $G = 200, 400 \text{ kg/m}^2\text{s}$, $p_1 = 8 \text{ MPa}$, $T_1 = 45, 36, 30 \text{ }^\circ\text{C}$, $q_w = 12 \text{ kW/m}^2$, (c) and (d) under the conditions: $TR = 3.78$, $G = 400 \text{ kg/m}^2\text{s}$, $q_w = 12 \text{ kW/m}^2$, $p_1 = 8, 9 \text{ MPa}$, (e) and (f) under the conditions: $TR = 3.78$, $G = 200 \text{ kg/m}^2\text{s}$, $q_w = 12, 24 \text{ kW/m}^2$, $p_1 = 8 \text{ MPa}$, (g) and (h) under the conditions: $TR = 2.17, 3.78$, $G = 200 \text{ kg/m}^2\text{s}$, $q_w = 12 \text{ kW/m}^2$, $p_1 = 8 \text{ MPa}$.

experimental data on the thermal-hydraulic performance of a TTI in a tube under SCO_2 flow conditions in the literature to validate the predicted friction factor and Nusselt number in the tube with the TTI. A large number of experiments on the friction factor and Nusselt number in tubes with TTIs exist when air or water was employed as a working fluid in the literature, but the thermal conditions such as inlet or outlet temperature, wall temperature or wall heat flux were not provided, hence a heat transfer simulation of TTIs cannot be conducted. Hopefully, the numerical results will be validated by using our own experimental data in the future. Second, the TTIs with $TR = 2.17, 3.78, 5.39$ were not perforated in this basic work. It is very hopeful this limitation can be turned down in the future. Third, the optimal TRs have been determined according to the $\psi\text{-}f/f_0$ curves predicted with CFD simulations. Nevertheless, these optimal TR values should be confirmed experimentally in the future. Fourth, the variation of TR is concerned only in the study. In

fact, a great number of factors such as TTI type, configuration, TR, tape aspect ratio, gap between the TTI tip and the tube wall, tape thickness, hole size of perforated tape and operational parameters etc can influence the thermal-hydraulic performance of TTIs. To sort out the complicated effects of those factors on thermal-hydraulic performance, the database of existing studies on TTIs should be analysed by employing machine learning method in the future. Applications of artificial neural network to the analysis of the thermal-hydraulic performance of solar air collectors [63], a solar air heater with circular perforated absorber plate [64], a triple concentric-tube HX with corrugated tubes [65] and HXs enhanced by delta-wing tape inserts [66] have provided excellent examples for that purpose.

Recently, a couple of different types of HXs have been investigated for the recuperator when SCO_2 is employed as the energy transport medium in power systems with the Brayton cycle, for instance, PCHES

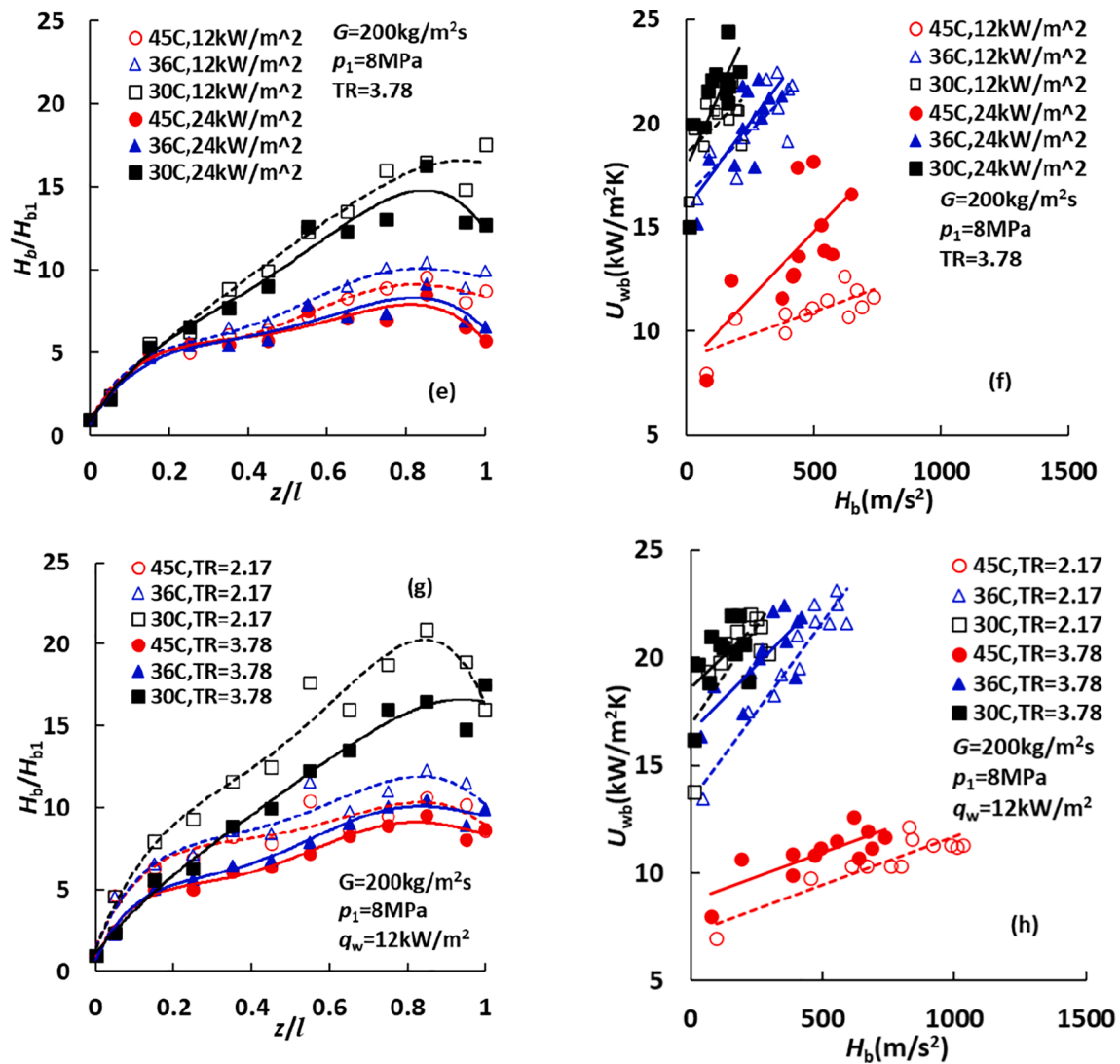


Fig. 15. (continued).

[67], HXs with serpentine channels [68] or coils [69], Kenics static mixer as HX [70], and minimal surface HXs [71]. Compared with PCHEs, minimal surface HXs suffer from less flow resistance, thus whether they can be adopted in water-cooled counter-flow tube-in-tube HXs of SCO₂ is worth being explored in the future.

5. Conclusions

For an experimental SCO₂ counter-flow tube-in-tube HX, the TTIs with different TRs were designed, and the convective heat transfer of SCO₂ flowing through the HX tube with a TTI was simulated in ANSYS CFX 2019R2 based on the 3D RANS flow and SST turbulence models at various SCO₂ inlet temperatures. The effects of TR, mass flux, inlet pressure and wall heat flux on the thermal-hydraulic performance of the TTIs were evaluated. The optimal TRs were identified for different flow and thermal conditions by means of the ψ curve and $f/f_0 \leq 5$ criterion. The thermal performance of the TTI was characterised in terms of cross-sectional average absolute helicity. It turned out that the SCO₂ thermophysical property has a dominant influence on Nu/Nu_0 and ψ curves. The maximum HTE occurs at the pseudocritical point and is around (2–3) folds better than the HTE under water or air flow conditions in terms of Nu/Nu_0 and ψ . The HTE drops off quickly on both the left- and right-hand sides of the point and approaches the HTE curves of water and air progressively based on Nu/Nu_0 and ψ . At the pseudocritical

point, $f/f_0=3.63\text{--}7.29$, $Nu/Nu_0=3.43\text{--}5.75$ and $\psi = 1.90\text{--}2.94$ are held in the inlet pressure of 8 MPa, mass flux of 200 kg/m²s and $q_w = 12\text{ kW/m}^2$ when TRs are in the values of 2.17, 3.78 and 5.39. An increased mass flux worsens the HTE on both sides of the pseudocritical point, especially on the left-hand side. An increased inlet pressure makes Nu/Nu_0 and ψ curves flat, thereby leading them to be closer to the Nu/Nu_0 and ψ curves of water and air. A large wall heat flux can raise the whole HTE curve insignificantly. The determination of optimal TR depends on SCO₂ operational conditions. TR = 3.78 likely is the optimal TR under the condition of $G = 200\text{ kg/m}^2\text{s}$, $p_1=8\text{ MPa}$ and $q_w = 12\text{ kW/m}^2$, while TR = 5.39 can be the optimal value for the condition of $G = 400\text{ kg/m}^2\text{s}$, $p_1=8, 9\text{ MPa}$ and $q_w = 12\text{ kW/m}^2$ or $G = 200\text{ kg/m}^2\text{s}$, $p_1=8\text{ MPa}$ and $q_w = 24\text{ kW/m}^2$. The cross-sectional mean wall heat transfer coefficient-absolute helicity curve can be used to characterise the thermal performance of a TTI. The water-cooled tube-in-tube HX with TTI for SCO₂ should work in a region near the pseudocritical point as close as possible to achieve the best HTE.

CRedit authorship contribution statement

Wenguang Li: Methodology, Software, Validation, Formal analysis, Data curation, Writing – original draft. **Zhibin Yu:** Conceptualization, Resources, Funding acquisition. **Yi Wang:** Writing – review & editing. **Yongliang Li:** Funding acquisition, Supervision, Project administration.

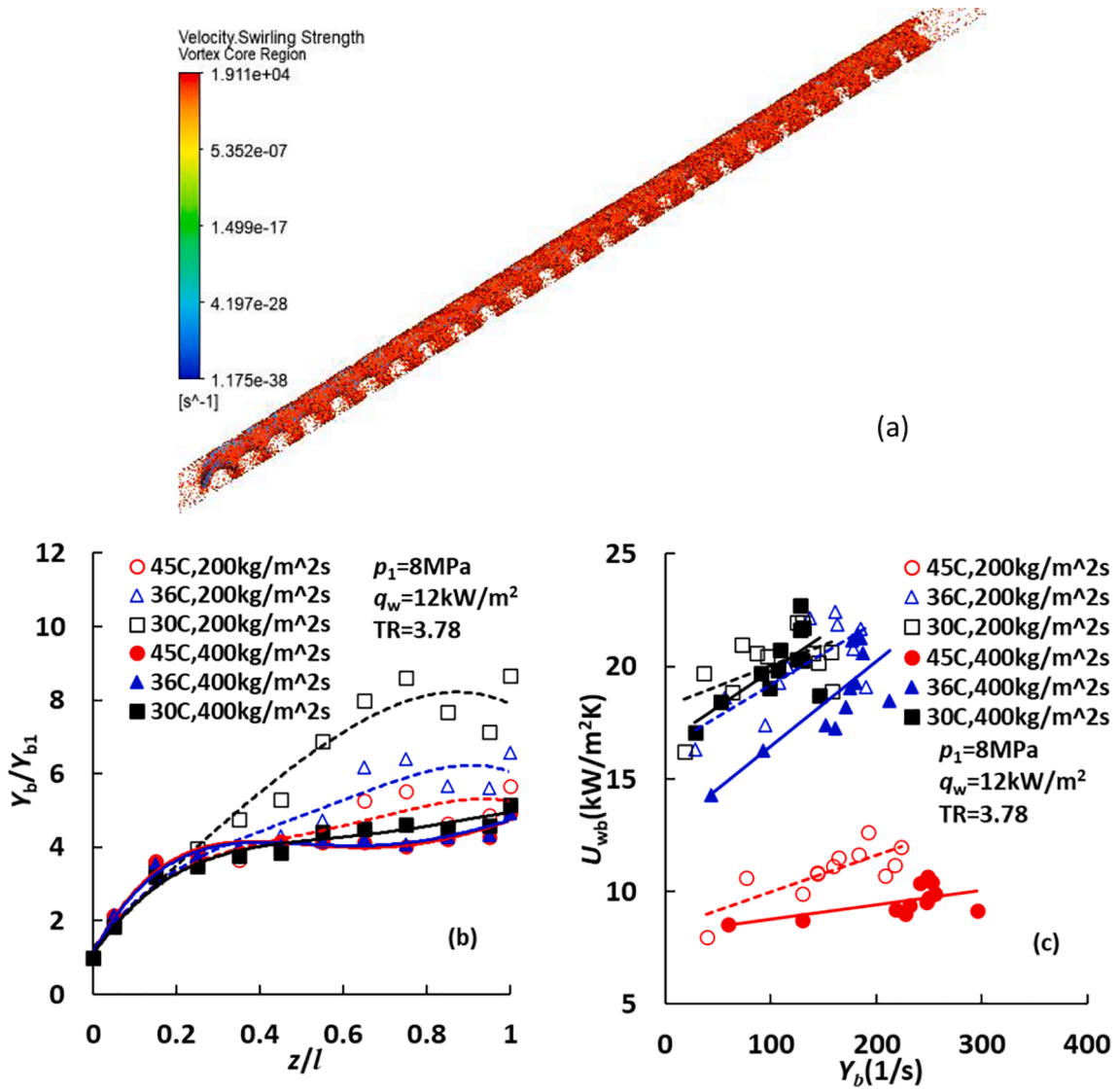


Fig. 16. The vortex region determined by the swirling strength Y at a threshold $Y = 396 s^{-1}$ (a), Y_b/Y_{b1} - z/l curves (b), and U_{wb} - Y_b curves (c) under the conditions: $TR = 3.78$, $G=200, 400 kg/m^2s$, $p_1=8 MPa$, $T_1=45, 36, 30 ^\circ C$, and $q_w = 24 kW/m^2$.

Declaration of Competing Interest

The authors declare that they have no known competing financial interests or personal relationships that could have appeared to influence the work reported in this paper.

Acknowledgements

The authors would like to acknowledge the financial support

provided by EPSRC (EP/T022701/1, EP/V042033/1, EP/V030515/1, EP/P028829/1, EP/N005228/1, EP/N020472/1) in the UK, and this project has also received funding from the European Union’s Horizon 2020 research and innovation programme under the Marie Skłodowska-Curie grant agreement No. 101007976.

Appendix A

The governing equations of flow and heat transfer models

For subsonic, compressible SCO_2 , the 3D RANS equations and energy equation with eddy viscosity turbulence models are written as [72].

$$\frac{\partial \rho}{\partial t} + \frac{\partial}{\partial x_j} (\rho u_j) = 0 \tag{A.1}$$

$$\frac{\partial}{\partial t} (\rho u_i) + \frac{\partial}{\partial x_j} (\rho u_i u_j) = -\frac{\partial}{\partial x_i} \left(p + \frac{2}{3} \rho k \right) + \frac{\partial}{\partial x_j} \left[(\mu + \mu_t) \left(\frac{\partial u_i}{\partial x_j} + \frac{\partial u_j}{\partial x_i} \right) \right] + S_i \tag{A.2}$$

$$\frac{\partial}{\partial t} \left[\rho \left(h + \frac{1}{2} u_i u_i + k \right) \right] - \frac{\partial p}{\partial t} + \frac{\partial}{\partial x_j} \left[\rho u_j \left(h + \frac{1}{2} u_i u_i + k \right) \right] = \frac{\partial}{\partial x_j} \left(\lambda \frac{\partial T}{\partial x_j} + \frac{\mu_t}{Pr_t} \frac{\partial h}{\partial x_j} \right) + S_E \quad (\text{A.3})$$

where ρ is the density of SCO_2 , t is time, u_i and u_j are the Reynolds or time-averaged velocity of SCO_2 in the coordinate x_i and x_j directions, respectively; i and j are the coordinate index, $i, j=1,2,3$; p is the pressure of SCO_2 , k is the turbulent kinetic energy, $k = \frac{1}{2} \overline{u_i^2}$, u_i is turbulent fluctuation velocity of SCO_2 , μ is the dynamic viscosity of SCO_2 ; μ_t is the turbulent eddy viscosity, S_i is the specific body force, $S_i = 0$ is held here, h is the enthalpy of SCO_2 , λ is the thermal conductivity of SCO_2 , T is the temperature of SCO_2 , Pr_t is the turbulent Prandtl number, $Pr_t=0.9$, S_E is the source term of energy, $S_E=0$ here; ρ , μ and λ are given by the RGP table.

The SST turbulence model was employed in the article. The SST model is a blended version of the Wilcox $k-\omega$ model and the standard $k-\epsilon$ model. The flow near the wall is handled by the Wilcox $k-\omega$ model, but the core flow is simulated by the standard $k-\epsilon$ model. To consider the transport of the shear stress, the overprediction of turbulent eddy viscosity is suppressed [73]. The Wilcox $k-\omega$ model reads as [72].

$$\frac{\partial}{\partial t} (\rho k) + \frac{\partial}{\partial x_j} (\rho u_j k) = \frac{\partial}{\partial x_j} \left[\left(\mu + \frac{\mu_t}{\sigma_{k1}} \right) \frac{\partial k}{\partial x_j} \right] + P_k - \beta_k \rho k \omega + P_{kb} \quad (\text{A.4})$$

$$\frac{\partial}{\partial t} (\rho \omega) + \frac{\partial}{\partial x_j} (\rho u_j \omega) = \frac{\partial}{\partial x_j} \left[\left(\mu + \frac{\mu_t}{\sigma_{\omega 1}} \right) \frac{\partial \omega}{\partial x_j} \right] + \frac{\alpha_1}{\nu_t} P_k - \beta_1 \rho k \omega^2 + P_{\omega b} \quad (\text{A.5})$$

where σ_{k1} , β_k , $\sigma_{\omega 1}$, α_1 and β_1 are the model constants, $\sigma_{k1}=\sigma_{\omega 1}=2$, $\alpha_1=5/9$, $\beta_k=0.09$, $\beta_1=0.075$; P_{kb} and $P_{\omega b}$ are the buoyancy production term in the k -equation and ω -equation, respectively; since the SCO_2 inlet temperature is low, the two production terms are ignored. The transformed standard $k-\epsilon$ model is written as:

$$\frac{\partial}{\partial t} (\rho k) + \frac{\partial}{\partial x_j} (\rho u_j k) = \frac{\partial}{\partial x_j} \left[\left(\mu + \frac{\mu_t}{\sigma_{k2}} \right) \frac{\partial k}{\partial x_j} \right] + P_k - \beta_k \rho k \omega + P_{kb} \quad (\text{A.6})$$

$$\frac{\partial}{\partial t} (\rho \omega) + \frac{\partial}{\partial x_j} (\rho u_j \omega) = \frac{\partial}{\partial x_j} \left[\left(\mu + \frac{\mu_t}{\sigma_{\omega 2}} \right) \frac{\partial \omega}{\partial x_j} \right] + \frac{\alpha_2}{\nu_t} P_k - \beta_2 \rho k \omega^2 + \frac{2\rho}{\sigma_{\omega 2} \omega} \frac{\partial k}{\partial x_j} \frac{\partial \omega}{\partial x_j} + P_{\omega b} \quad (\text{A.7})$$

where σ_{k2} , $\sigma_{\omega 2}$, α_2 and β_2 are the model constants, $\sigma_{k2}=1$, $\sigma_{\omega 2}=1/0.856$, $\alpha_2=0.44$, $\beta_2=0.0828$.

By using a blending function F_1 , Eq.(A.4) and (A.6), Eq.(A.5) and (A.7) are combined in such a way: $F_1 \times$ Eq. (A.4) + $(1 - F_1) \times$ Eq. (A.6) and $F_1 \times$ Eq. (A.5) + $(1 - F_1) \times$ Eq. (A.7), respectively, then the blended $k-\omega$ model is obtained:

$$\frac{\partial}{\partial t} (\rho k) + \frac{\partial}{\partial x_j} (\rho u_j k) = \frac{\partial}{\partial x_j} \left[\left(\mu + \frac{\mu_t}{\sigma_{k3}} \right) \frac{\partial k}{\partial x_j} \right] + P_k - \beta_k \rho k \omega + P_{kb} \quad (\text{A.8})$$

$$\frac{\partial}{\partial t} (\rho \omega) + \frac{\partial}{\partial x_j} (\rho u_j \omega) = \frac{\partial}{\partial x_j} \left[\left(\mu + \frac{\mu_t}{\sigma_{\omega 3}} \right) \frac{\partial \omega}{\partial x_j} \right] + \frac{\alpha_3}{\nu_t} P_k - \beta_3 \rho k \omega^2 + (1 - F_1) \frac{2\rho}{\sigma_{\omega 2} \omega} \frac{\partial k}{\partial x_j} \frac{\partial \omega}{\partial x_j} + P_{\omega b} \quad (\text{A.9})$$

where σ_{k3} , $\sigma_{\omega 3}$, α_3 and β_3 are the blended model constants, expressed as $\sigma_{k3}=F_1 \sigma_{k1} + \beta_1 (1-F_1) \sigma_{k2}$, $\sigma_{\omega 3}=F_1 \sigma_{\omega 1} + (1-F_1) \sigma_{\omega 2}$, $\alpha_3=F_1 \alpha_1 + (1-F_1) \alpha_2$, and $\beta_3=F_1 \beta_1 + (1-F_1) \beta_2$; F_1 is a blending function between the Wilcox $k-\omega$ model and the standard $k-\epsilon$ model, especially, $F_1=1$ at the wall, $F_1=0$ in the core flow, and $0 < F_1 < 1$ between the wall and the core flow. A specific expression for F_1 is written as [72,73]:

$$F_1 = \tanh(\xi_1^4), \xi_1 = \min \left(\max \left(\frac{\sqrt{k}}{\beta_k \omega y_n}, \frac{500\nu}{y_n^2 \omega} \right), \frac{4\rho k}{\xi_2 \sigma_{\omega 2} y_n^2} \right), \xi_2 = \max \left(\frac{2\rho}{\sigma_{\omega 2} \omega} \frac{\partial k}{\partial x_j} \frac{\partial \omega}{\partial x_j}, 1.0 \times 10^{-10} \right) \quad (\text{A.10})$$

where ν is the kinematic viscosity of SCO_2 , y_n is the distance the nearest wall.

To take the SST into account, the eddy viscosity should be limited in a manner. In [73], a mathematical expression was proposed to remove the overprediction of the eddy viscosity, i.e.

$$\mu_t = \min \left(\frac{\rho k}{\omega}, \frac{a_1 \rho k}{\gamma F_2} \right), \gamma = \sqrt{2\gamma_{ij} \gamma_{ij}}, \gamma_{ij} = \frac{1}{2} \left(\frac{\partial u_i}{\partial x_j} + \frac{\partial u_j}{\partial x_i} \right), F_2 = \tanh(\xi_2^2), \xi_2 = \max \left(\frac{2\sqrt{k}}{\beta_k \omega y_n}, \frac{500\nu}{y_n^2 \omega} \right) \quad (\text{A.11})$$

where a_1 is a constant, $a_1 = 0.31$, γ is the magnitude of the strain rate and γ_{ij} represents the strain rate tensor. In ANSYS CFX, the model composed by Eqs. (A.8)–(A.11) is the SST model.

In the SST model, the low-Reynolds number model for the viscous sublayer is replaced with a blended wall function, which is called Automatic Near-Wall Treatment in ANSYS CFX. The blended wall function is a function of $y^+ (=u_\tau y_n / \nu)$, u_τ denotes the friction velocity of SCO_2 at wall and related to the wall shear stress with $\tau_w = \rho u_\tau^2$. The blended wall function, which is focused on both ω and u_τ , is based on the solutions in the linear and the logarithmic near-wall regions, and written as [73]:

$$\begin{cases} \omega_n = \sqrt{\omega_{vis}^2 + \omega_{log}^2}, \omega_{vis} = \frac{6\nu}{\beta_1 y_n^2}, \omega_{log} = \frac{u_\tau}{a_1 \kappa y_n} \\ u_\tau = \sqrt{(u_\tau^{vis})^4 + (u_\tau^{log})^4}, u_\tau^{vis} = \frac{u_n}{y^+}, u_\tau^{log} = \frac{u_n}{\frac{1}{\kappa} \ln(y^+) + B} \end{cases} \quad (\text{A.12})$$

where ω_{vis} and ω_{log} are the ω values calculated by the solutions in the linear and the logarithmic near-wall regions, ω_n is the total ω near wall, u_τ^{vis} and

u_{τ}^{log} are the friction velocities at wall by using the solutions in the sublayer linear and logarithmic law layers, u_n is the fluid velocity near wall, B is a constant, $B=5.2$ for hydraulically smooth walls. The fluxes in the momentum equation and the k -equation at wall are detailed in [72].

In the sublayer linear and logarithmic law regions, the following empirical expression in [74] is employed in CFX to determine the dimensionless temperature in convective heat transfer [73,74]:

$$\begin{cases} T^+ = Pr y^+ e^{-\Gamma} + [0.11 \ln(y^+) + \beta] e^{-1/\Gamma}, \Gamma = \frac{0.01 (Pr y^+)^4}{1 + 5 Pr^3 y^+} \\ q_w = \frac{\rho c_p \mu_{\tau}}{T^+} (T_w - T_n), Pr = \frac{\mu c_p}{\lambda}, \beta = (3.85 Pr^{1/3} - 1.3) + 0.11 \ln(Pr) \end{cases} \quad (A.13)$$

where Γ is the auxiliary variable of Pr and y^+ , q_w is the wall heat flux, c_p is the specific heat capacity of SCO_2 , T^+ is the dimensionless temperature in the boundary layer, T_w is the wall temperature, T_n is the SCO_2 temperature in the first mesh layer, β is the model constant, Pr is the SCO_2 Prandtl number; the SCO_2 property constants, ρ , μ , c_p and λ should be the local values in the first mesh layer. Based on Eqs. (A.12) and (A.13), the flow and heat transfer variables at wall, e.g., shear stress, wall temperature or heat flux can be calculated.

Appendix B

Mathematics of absolute helicity and vorticity

The fluid velocity vector \mathbf{u} , velocity gradient tensor $\nabla \mathbf{u}$ and vorticity vector $\nabla \times \mathbf{u}$ are defined as follows:

$$\mathbf{u} = [u_1, u_2, u_3], \nabla \mathbf{u} = \begin{bmatrix} \frac{\partial u_1}{\partial x_1} & \frac{\partial u_1}{\partial x_2} & \frac{\partial u_1}{\partial x_3} \\ \frac{\partial u_2}{\partial x_1} & \frac{\partial u_2}{\partial x_2} & \frac{\partial u_2}{\partial x_3} \\ \frac{\partial u_3}{\partial x_1} & \frac{\partial u_3}{\partial x_2} & \frac{\partial u_3}{\partial x_3} \end{bmatrix}, \nabla \times \mathbf{u} = \left[\frac{\partial u_3}{\partial x_2} - \frac{\partial u_2}{\partial x_3}, \frac{\partial u_1}{\partial x_3} - \frac{\partial u_3}{\partial x_1}, \frac{\partial u_2}{\partial x_1} - \frac{\partial u_1}{\partial x_2} \right] \quad (B.1)$$

Roughly, there are two methods to examine kinematics of vortex [61]. The first one is based on \mathbf{u} and $\nabla \times \mathbf{u}$, the second one is based on the eigenvalues of $\nabla \times \mathbf{u}$. The absolute helicity in [61] belongs to the first method, and is expressed by the following scalar:

$$H = |\mathbf{u} \bullet (\nabla \times \mathbf{u})| = \left| u_1 \left(\frac{\partial u_3}{\partial x_2} - \frac{\partial u_2}{\partial x_3} \right) + u_2 \left(\frac{\partial u_1}{\partial x_3} - \frac{\partial u_3}{\partial x_1} \right) + u_3 \left(\frac{\partial u_2}{\partial x_1} - \frac{\partial u_1}{\partial x_2} \right) \right| \quad (B.2)$$

This method is simple and easily understood. We can illustrate the vortex shape by plotting iso-surfaces of the helicity in a flow field.

The vorticity or velocity curl Ω is the magnitude of the vorticity vector $\nabla \times \mathbf{u}$, and expressed by.

$$\Omega = \sqrt{\left(\frac{\partial u_3}{\partial x_2} - \frac{\partial u_2}{\partial x_3} \right)^2 + \left(\frac{\partial u_1}{\partial x_3} - \frac{\partial u_3}{\partial x_1} \right)^2 + \left(\frac{\partial u_2}{\partial x_1} - \frac{\partial u_1}{\partial x_2} \right)^2} \quad (B.3)$$

The swirling strength is originated from the analysis of eigenvalues of the velocity gradient tensor $\nabla \mathbf{u}$. The swirling strength should belong to the second method mentioned above and can be used to specify the vortex shape. There are three invariants in $\nabla \mathbf{u}$. The invariants are exactly the coefficients of a 3rd-order polynomial that the eigenvalues satisfy. These invariants are written as:

$$\begin{cases} I_1 = -\text{tr}(\nabla \mathbf{u}) = -\frac{\partial u_i}{\partial x_i} \\ I_2 = \frac{1}{2} [J_1^2 - \text{tr}(\nabla \mathbf{u} \nabla \mathbf{u})] = \frac{1}{2} \left[\left(\frac{\partial u_i}{\partial x_i} \right)^2 - \frac{\partial u_i}{\partial x_j} \frac{\partial u_j}{\partial x_i} \right] \\ I_3 = -\det(\nabla \mathbf{u}) = \epsilon_{ijm} \frac{\partial u_1}{\partial x_i} \frac{\partial u_2}{\partial x_j} \frac{\partial u_3}{\partial x_m}, i, j, m = 1, 2, 3 \end{cases} \quad (B.4)$$

where the $\text{tr}(\nabla \mathbf{u})$ is the sum of the diagonal entries of $\nabla \mathbf{u}$, likewise, $\text{tr}(\nabla \mathbf{u} \nabla \mathbf{u})$ is the sum of the diagonal elements of $\nabla \mathbf{u} \nabla \mathbf{u}$; ϵ_{ijm} are the Levi-Civita symbol, if let $i, j, m = 1, 2, 3$, then $\epsilon_{123} = \epsilon_{312} = \epsilon_{231} = 1$, $\epsilon_{132} = \epsilon_{321} = \epsilon_{213} = -1$, otherwise $\epsilon_{ijm} = 0$; the $\det(\nabla \mathbf{u})$ is the determinant of $\nabla \mathbf{u}$. Three invariants define a discriminant as follows [60,61]:

$$\Delta = \left(-\frac{I_1^2}{9} + \frac{I_2}{3} \right)^3 + \left(\frac{I_1^3}{27} - \frac{I_1 I_2}{6} + \frac{I_3}{2} \right)^2 \quad (B.5)$$

When $\Delta > 0$, $\nabla \mathbf{u}$ is subject to one real and two complex conjugate eigenvalues, and their imaginary part stands for the swirling strength of the vortex. The swirling strength is expressed by [60].

$$Y = \frac{\sqrt{3}}{2} \left[\sqrt{\sqrt{\Delta} - \left(\frac{I_1^3}{27} - \frac{I_1 I_2}{6} + \frac{I_3}{2} \right)} + \sqrt{\sqrt{\Delta} + \left(\frac{I_1^3}{27} - \frac{I_1 I_2}{6} + \frac{I_3}{2} \right)} \right] \quad (B.6)$$

The other methods for identifying vortex shape can be found in [61], and are not repeated here.

References

- [1] K. Kuwahara, S. Higashiue, D. Ito, et al., Experimental study on cooling heat transfer of supercritical carbon dioxide inside horizontal micro-fin tubes, *Trans. JSRAE* 24 (3) (2007) 173–181.
- [2] H.S. Lee, H.J. Kim, J.I. Yoon, et al., The cooling heat transfer characteristics of the supercritical CO₂ in micro-fin tube, *Heat Mass Transf.* 49 (2013) 173–184.
- [3] G. Xie, J. Liu, P.M. Ligrani, et al., Numerical analysis of flow structure and heat transfer characteristics in square channels with different internal-protruded dimple geometries, *Int. J. Heat Mass Transf.* 67 (2013) 81–97.
- [4] H.S. Yoon, S.H. Park, C. Choi, et al., Numerical study on characteristics of flow and heat transfer in a cooling passage with a tear-drop dimple surface, *Int. J. Therm. Sci.* 89 (2015) 121–135.
- [5] Y. Xie, H. Qu, D. Zhang, Numerical investigation of flow and heat transfer in rectangular channel with teardrop dimple/protrusion, *Int. J. Heat Mass Transf.* 84 (2015) 486–496.
- [6] Y. Rao, B. Li, Y. Feng, Heat transfer of turbulent flow over surfaces with spherical dimples and teardrop dimples, *Exp. Therm. Fluid Sci.* 61 (2015) 201–209.
- [7] S.A. Isaev, A.V. Schelchikov, A.I. Leontiev, et al., Numerical simulation of the turbulent air flow in the narrow channel with a heated wall and a spherical dimple placed on it for vortex heat transfer enhancement depending on the dimple depth, *Int. J. Heat Mass Transf.* 94 (2016) 426–448.
- [8] M. Li, T.S. Khan, E. Al-Hajri, et al., Single phase heat transfer and pressure drop analysis of a dimpled enhanced tube, *Appl. Therm. Eng.* 101 (2016) 38–46.
- [9] S. Xie, Z. Liang, L. Zhang, et al., Numerical investigation on heat transfer performance and flow characteristics in enhanced tube with dimples and protrusions, *Int. J. Heat Mass Transf.* 122 (2018) 602–613.
- [10] S. Xie, Z. Liang, L. Zhang, et al., A numerical study on heat transfer enhancement and flow structure in enhanced tube with cross ellipsoidal dimples, *Int. J. Heat Mass Transf.* 125 (2018) 434–444.
- [11] L. Zhang, S. Xie, Z. Liang, et al., Numerical investigation of flow and heat transfer in enhanced tube with slot dimples, *Heat Mass Transf.* 55 (2019) 3697–3709.
- [12] R.B. Manoram, R.S. Moorthy, R. Ragunathan, Investigation on influence of dimpled surfaces on heat transfer enhancement and friction factor in solar water heater, *J. Thermal Anal. Calorimet. Vols.* (2020), <https://doi.org/10.1007/s10973-020-09746-0>.
- [13] A. Firoozi, S. Majidi, M. Ameri, A numerical assessment on heat transfer and flow characteristics of nanofluid in tubes enhanced with a variety of dimple configurations, *Therm. Sci. Eng. Prog.* 19 (2020), 100578.
- [14] B. Lotfi, B. Sunden, Thermo-hydraulic performance enhancement of finned elliptical tube heat exchangers by utilizing innovative dimple turbulators, *Heat Transfer Eng.* 41 (13) (2020) 1117–1142.
- [15] S. Eiamsa-ard, K. Wongcharee, S. Sripattanapit, 3-D Numerical simulation of swirling flow and convective heat transfer in a circular tube induced by means of loose-fit twisted tapes, *Int. Commun. Heat Mass Transfer* 36 (2009) 947–955.
- [16] S. Alzahrani, S. Usman, CFD simulations of the effect of in-tube twisted tape design on heat transfer and pressure drop in natural circulation, *Therm. Sci. Eng. Prog.* 18 (2019) 325–333.
- [17] S. Eiamsa-ard, K. Kiatkittipong, Heat transfer enhancement by multiple twisted tape inserts and TiO₂/water nanofluid, *Appl. Therm. Eng.* 70 (2014) 896–924.
- [18] A.T. Wijayanta, Mirmanto, M. Aziz, Heat transfer augmentation of internal flow using twisted tape insert in turbulent flow, *Heat Transfer Eng.* 41 (2020) 1288–1300.
- [19] P. Li, Z. Liu, W. Liu, et al., Numerical study on heat transfer enhancement characteristics of tube inserted with centrally hollow narrow twisted tapes, *Int. J. Heat Mass Transf.* 88 (2015) 481–491.
- [20] X. Liu, C. Li, X. Cao, et al., Numerical analysis on enhanced performance of new coaxial cross twisted tapes for laminar convective heat transfer, *Int. J. Heat Mass Transf.* 121 (2018) 1125–1136.
- [21] N.M. Zade, S. Akar, S. Rashidi, et al., Thermo-hydraulic analysis for a novel eccentric helical screw tape insert in a three dimensional tube, *Appl. Therm. Eng.* 124 (2017) 413–421.
- [22] S.R. Chaurasia, R.M. Sarviya, Numerical and experimental thermal performance with entropy generation analysis on tube with helical screw tape inserts at number of strips in turbulent flow, *Proc IMechE Part C: Journal of Mechanical Engineering Science* 235 (6) (2021) 1057–1070.
- [23] T.O. Oni, M. Paul, Numerical investigation of heat transfer and fluid flow of water through a circular tube induced with divers' tape inserts, *Appl. Therm. Eng.* 98 (2016) 157–168.
- [24] S.A. Sowi, S. Abdullah, K. Sopian, The effect of linearly increasing/decreasing pitch ratio twisted tape with various progression rate and nanofluid towards the system performance, *Therm. Sci. Eng. Prog.* 20 (2021), 100979.
- [25] S. Eiamsa-ard, P. Promthaisong, C. Thianpong, Influence of three-start spirally twisted tube combined with triple-channel twisted tape insert on heat transfer enhancement, *Chem. Eng. Process. Process Intensif.* 102 (2016) 117–129.
- [26] N.T.R. Ravi Kumara, Bhramara, A. Kirubeil, et al., Effect of twisted tape inserts on heat transfer, friction factor of Fe₃O₄ nanofluids flow in a double pipe U-bend heat exchanger, *Int. Commun. Heat Mass Transfer* 95 (2018) 53–62.
- [27] S.P. Nalavade, C.L. Prabhune, N.K. Sane, Effect of novel flow divider type turbulators on fluid flow and heat transfer, *Therm. Sci. Eng. Prog.* 9 (2019) 322–331.
- [28] A. Kumar, A. Layek, Thermo-hydraulic performance of roughened solar air heater by design of experiment and meta-heuristic approach, *Therm. Sci. Eng. Prog.* 10 (2019) 92–102.
- [29] Y. Liu, X. Ma, X. Ye, Heat transfer enhancement of annular finned tube exchanger using vortex generators: The effect of oriented functional circumferential arrangement, *Therm. Sci. Eng. Prog.* 10 (2019) 27–35.
- [30] Y. Xu, M.D. Islam, N. Kharoua, Numerical study of winglets vortex generator effects on thermal performance in a circular pipe, *Int. J. Therm. Sci.* 112 (2017) 304–317.
- [31] S. Biswakarma, S. Roy, B. Dasa, et al., Performance analysis of internally helically v-grooved absorber tubes using nanofluid, *Therm. Sci. Eng. Prog.* 18 (2020), 100538.
- [32] N. Cheriet, H. Amirat, A. Korichi, et al., Conjugate heat transfer enhancement over heated blocks using airfoil deflectors, *Therm. Sci. Eng. Prog.* 25 (2021), 101011.
- [33] S. Salari, K. Goudarzi, Intensification of heat transfer in heater tubes of city gas stations using spiral spring inserts, *Therm. Sci. Eng. Prog.* 3 (2017) 123–132.
- [34] H.A. Mohammed, H.A. Hasan, M.A. Wahid, Heat transfer enhancement of nanofluids in a double pipe heat exchanger with louvered strip inserts, *Int. Commun. Heat Mass Transfer* 40 (2013) 36–46.
- [35] L.S. Sundar, Z. Said, B. Saleh, et al., Combination of Co₃O₄ deposited rGO hybrid nanofluids and longitudinal strip inserts: Thermal properties, heat transfer, friction factor, and thermal performance evaluations, *Therm. Sci. Eng. Prog.* 20 (2020), 100695.
- [36] H.A. Mohammed, A.K. Abbas, J.M. Sherif, Influence of geometrical parameters and forced convective heat transfer in transversely corrugated circular tubes, *Int. Commun. Heat Mass Transfer* 44 (2013) 116–126.
- [37] T. Alam, M.H. Kim, Heat transfer enhancement in solar air heater duct with conical protrusion roughness ribs, *Appl. Therm. Eng.* 126 (2017) 458–469.
- [38] S. Singh, H. Kharkwal, A. Gautam, et al., CFD analysis for thermo-hydraulic properties in a tubular heat exchanger using curved circular rings, *J. Therm. Anal. Calorim.* 141 (2020) 2211–2218.
- [39] M. Awais, A.A. Bhuiyan, Heat transfer enhancement using different types of vortex generators (VGs): A review on experimental and numerical activities, *Therm. Sci. Eng. Prog.* 5 (2018) 524–545.
- [40] C. Bi, G.H. Tang, W.Q. Tao, Heat transfer enhancement in mini-channel heat sinks with dimples and cylindrical grooves, *Appl. Therm. Eng.* 55 (2013) 121–132.
- [41] A. Kaood, T. Abou-Deif, H. Eltahan, et al., Numerical investigation of heat transfer and friction characteristics for turbulent flow in various corrugated tubes, *Proc IMechE Part A: J. Power Energy* 233 (4) (2019) 457–475.
- [42] A.R. Al-Obaidi, Analysis of the flow field, thermal performance, and heat transfer augmentation in circular tube using different dimple geometrical configurations with internal twisted-tape insert, *Heat Transfer* 49 (2020) 4153–4172.
- [43] H. Arjmandi, P. Amiri, M.S. Pour, Geometric optimization of a double pipe heat exchanger with combined vortex generator and twisted tape: A CFD and response surface methodology (RSM) study, *Therm. Sci. Eng. Prog.* 18 (2020), 100514.
- [44] M.M. Bhuiya, M.S. Chowdhury, M. Saha, et al., Heat transfer and friction factor characteristics in turbulent flow through a tube fitted with perforated twisted tape inserts, *Int. Commun. Heat Mass Transfer* 46 (2013) 49–57.
- [45] W. Li, Z. Yu, Heat exchangers for cooling supercritical carbon dioxide and heat transfer enhancement: A review and assessment, *Energy Rep.* 7 (2021) 4085–4105.
- [46] R.K. Shah, D.P. Sekulic, Fundamentals of Heat Exchanger Design, John Wiley & Sons Inc, Hoboken, 2003.
- [47] S. Ponnada, T. Subrahmanyam, S.V. Naidu, A comparative study on the thermal performance of water in a circular tube with twisted tapes, perforated twisted tapes and perforated twisted tapes with alternate axis, *Int. J. Therm. Sci.* 136 (2019) 530–538.
- [48] H. Bas, V. Ozceyhan, Heat transfer enhancement in a tube with twisted tape inserts placed separately from the tube wall, *Exp. Therm. Fluid Sci.* 41 (2012) 51–58.
- [49] P. Murugesan, K. Mayilsamy, S. Suresh, Turbulent heat transfer and pressure drop in tube fitted with square-cut twisted tape, *Chin. J. Chem. Eng.* 18 (4) (2010) 609–617.
- [50] N. Piriyaarungrod, S. Eiamsa-ard, C. Thianpong, et al., Heat transfer enhancement by tapered twisted tape inserts, *Chem. Eng. Process. Process Intensif.* 96 (2015) 62–71.
- [51] S. Eiamsa-ard, K. Wongcharee, K. Kunrak, et al., Heat transfer enhancement of TiO₂-water nanofluid flow in dimpled tube with twisted tape insert, *Heat Mass Transf.* 55 (2019) 2987–3001.
- [52] D. Kumbhar, N.K. Sane, Exploring heat transfer and friction factor performance of a dimpled tube equipped with regularly spaced twisted tape inserts, *Procedia Eng.* 127 (2015) 1142–1149.
- [53] M. Kosker, F. Yilmaz, The cross-sectional curvature effect of twisted tapes on heat transfer performance, *Chem. Eng. Process. Process Intensif.* 154 (2020), 108008.
- [54] C. Thianpong, P. Eiamsa-ard, K. Wongcharee, et al., Compound heat transfer enhancement of a dimpled tube with a twisted tape swirl generator, *Int. Commun. Heat Mass Transfer* 36 (2009) 798–804.
- [55] M. Hazbehian, H. Maddah, H. Mohammadi, et al., Experimental investigation of heat transfer augmentation inside double pipe heat exchanger equipped with reduced width twisted tapes inserts using polymeric nanofluid, *Heat Mass Transf.* 52 (2016) 2515–2529.
- [56] W. Li, Z. Yu, Y. Wang, et al., Heat transfer of supercritical carbon dioxide in a tube-in-tube heat exchanger-A CFD study, *J. Supercrit. Fluids*, 181, pp. 105493-1-18, 2022.
- [57] C. Dang, E. Hihara, In-tube cooling heat transfer of supercritical carbon dioxide. Part 1. Experimental measurement, *Int. J. Refrig* 27 (2004) 736–747.
- [58] Z. Du, W. Lin, A. Gu, Numerical investigation of cooling heat transfer to supercritical CO₂ in a horizontal circular tube, *J. Supercrit. Fluids* 55 (2010) 116–121.
- [59] M. Xiang, J. Guo, X. Huai, et al., Thermal analysis of supercritical pressure CO₂ in horizontal tubes under cooling condition, *J. Supercrit. Fluids* 130 (2017) 389–398.
- [60] ANSYS, ANSYS CFX-Post User's Guide, ANSYS Inc, Canonsburg, 2012.

- [61] S. Zhang, D. Choudhury, Eigen helicity density: A new vortex identification scheme and its application in accelerated inhomogeneous flows, *Phys. Fluids* 18 (2006), 058104.
- [62] ANSYS, ANSYS CFX-Solver Modeling Guide, ANSYS Inc, Canonsburg, 2011.
- [63] M. Caner, E. Gedik, A. Keçebas, Investigation on thermal performance calculation of two type solar air collectors using artificial neural network, *Expert Syst. Appl.* 38 (2011) 1668–1674.
- [64] S.P. Shetty, S. Nayak, S. Kumar, et al., Thermo-hydraulic performance prediction of a solar air heater with circular perforated absorber plate using Artificial Neural Network, *Therm. Sci. Eng. Prog.* 23 (2021), 100886.
- [65] J.D. Moya-Rico, A.E. Molina, J.F. Belmonte, et al., Characterization of a triple concentric-tube heat exchanger with corrugated tubes using Artificial Neural Networks (ANN), *Appl. Therm. Eng.* 147 (2019) 1036–1046.
- [66] M.Z.A. Khan, M. Aziz, A.T. Wijayanta, Prediction of heat transfer enhancement of delta-wing tape inserts using artificial neural network, *Case Stud. Therm. Eng.* 27 (2021), 101322.
- [67] T.H. Kim, J.G. Kwon, S.H. Yoon, et al., Numerical analysis of air-foil shaped fin performance in printed circuit heat exchanger in a supercritical carbon dioxide power cycle, *Nucl. Eng. Des.* 288 (2015) 110–118.
- [68] X. Cui, J. Guo, X. Huai, et al., Numerical investigations on serpentine channel for supercritical CO₂ recuperator, *Energy* 172 (2019) 517–530.
- [69] K. Wang, X. Xu, Y. Wu, et al., Numerical investigation on heat transfer of supercritical CO₂ in heated helically coiled tubes, *J. Supercrit. Fluids* 99 (2015) 112–120.
- [70] P.F. Lisboa, J. Fernandes, P.C. Simões, et al., Computational-fluid-dynamics study of a Kenics static mixer as a heat exchanger for supercritical carbon dioxide, *J. Supercrit. Fluids* 55 (2010) 107–115.
- [71] W. Li, G. Yu, Z. Yu, Bioinspired heat exchangers based on triply periodic minimal surfaces for supercritical CO₂ cycles, *Appl. Therm. Eng.* 179 (2020), 115686.
- [72] ANSYS, ANSYS CFX-Solver Theory Guide, ANSYS Inc, Canonsburg, 2011.
- [73] F. Menter, J.C. Ferreira, T. Esch, et al., The SST turbulence model with improved wall treatment for heat transfer predictions in gas turbines. in *Proceedings of the International Gas Turbine Congress*, 2003.
- [74] B.A. Kader, Temperature and concentration profiles in fully turbulent boundary layers, *Int. J. Heat Mass Transf.* 24 (9) (1981) 1541–1544.